J. Fluid Mech. (1994), vol. 281, pp. 51–80

Self-diffusion of bimodal suspensions of hydrodynamically interacting spherical particles in shearing flow

By CHINGYI CHANG AND ROBERT L. POWELL
Department of Chemical Engineering, University of California at Davis, Davis, CA 95616, USA

(Received 30 April 1993 and in revised form 31 March 1994)

We study the average mobilities and long-time self-diffusion coefficients of a suspension of bimodally distributed spherical particles. Stokesian dynamics is used to calculate the particle trajectories for a monolayer of bimodal-sized spheres. Hydrodynamic forces only are considered and they are calculated using the inverse of the grand mobility matrix for far-field many-body interactions and lubrication formulae for near-field effects. We determine both the detailed microstructure (e.g. the pair-connectedness function and cluster formation) and the macroscopic properties (e.g. viscosity and self-diffusion coefficients). The flow of an 'infinite' suspension is simulated by considering 25, 49, 64 and 100 particles to be one 'cell' of a periodic array. Effects of both the size ratio and the relative fractions of the different-sized particles are examined. For the microstructures, the pair-connectedness function shows that the particles form clusters in simple shearing flow due to lubrication forces. The nearly symmetric angular structures imply the absence of normal stress differences for a suspension with purely hydrodynamic interactions between spheres. For average mobilities at infinite Péclet number, D_0^s, our simulation results suggest that the reduction of D_0^s as concentration increases is directly linked to the influence of particle size distribution on the average cluster size. For long-time self-diffusion coefficients, D_∞^s, we found good agreement between simulation and experiment (Leighton & Acrovos 1987*a*; Phan and Leighton 1993) for monodispersed suspensions. For bimodal suspensions, the magnitude of D_∞^s, and the time to reach the asymptotic diffusive behaviour depend on the cluster size formed in the system, or the viscosity of the suspension. We also consider the effect of the initial configuration by letting the spheres be both organized (size segregated) and randomly placed. We find that it takes a longer time for a suspension with an initially organized structure to achieve steady state than one with a random structure.

1. Introduction

Over the last two decades, our understanding of the microrheological and transport properties of non-dilute suspensions of spherical particles has benefited from several experimental and theoretical advances. Computational methods have evolved that permit the determination of the dynamics of suspension microstructures due to an imposed flow or force, even at particle concentrations near maximum packing. Concomitantly, transport properties, for example, the relative shear viscosity, can be predicted (Brady & Bossis 1988). Nearly all of this work has focused on suspensions of monodispersed spherical particles. From a practical standpoint, most suspensions are composed of particles of various shapes and sizes. Even in suspensions composed of approximately spherical particles, at very high volume loadings it is usually desirable to have a distribution of particle sizes to aid in processing (Miller, Lee & Powell 1991). In a recent study (Chang & Powell 1993), we have shown that the rheological properties of suspensions of bimodally distributed spherical particles could be predicted using Stokesian dynamics (Brady & Bossis 1988). In this paper, by using simulations of a monolayer, we expand these results to include predictions of suspension microstructure and other transport properties, such as shear-induced diffusivities.

Recent experimental work has led to conclusive evidence for 'shear-induced hydrodynamic diffusion' (e.g. Eckstein, Bailey & Shapiro 1977; Gadala-Maria & Acrivos 1980; Graham *et al.* 1991; Abbott *et al.* 1991; Leighton & Acrivos 1987*a*, *b*; Nadim 1988; Koch 1989; Phillips *et al.* 1992; Phan & Leighton 1993). This effect exists at high Péclet numbers, *Pe*, when Brownian diffusion effects are insignificant; and at low particle Reynolds numbers, *Re*, when inertial effects are precluded. Hence, shear-induced hydrodynamic diffusion is unrelated to either the random thermal motion of fluid molecules surrounding each particle, or particle drift during flow due to inertial forces.

Different mechanisms cause particles in a suspension to migrate from one region to another solely by hydrodynamic forces (Leighton & Acrivos 1987*a*, *b*; Phillips *et al.* 1992). In flows with shear rate gradients, particles drift from regions of high shear rate to regions of low shear rate (Abbott *et al.* 1991). Concentration gradients cause the migration of spheres through two mechanisms. One is attributed to irreversible interactions between particles that result from even slight surface roughness of the particles, while the other comes from the spatially varying viscosity due to the gradients in the particle concentration (Leighton & Acrivos 1987*b*; Phillips *et al.* 1992).

Another mechanism that causes the drift of spheres, which is addressed in this paper, is due to many-body hydrodynamic interactions among the particles under shearing flow (Eckstein *et al.* 1977; Leighton & Acrivos 1987*a*; Phan & Leighton 1993). For this 'shear-induced self-diffusion', a single 'tracer' sphere in a homogeneous suspension undergoing simple shearing flow interacts with its neighbours, and experiences a series of displacements normal to the streamlines of the macroscopic shearing flow. These displacements are random with zero mean (i.e. on average the particle will remain on its initial streamline). The test particle experiences a random walk process that is akin to classical self-diffusion but which, in this case, is shear-induced. In the presence of a concentration gradient, such a random walk leads to a diffusive flux that may be characterized by a diffusion coefficient (see below). One should note that in dilute suspensions of large perfectly smooth spheres, the particles return to their initial streamlines at the end of all two-particle interactions owing to linearity of the viscous-flow equations. At least three particles must interact to yield the permanent displacements that lead to a random walk with non-zero mean.

The self-diffusion process for hydrodynamically interacting spherical particles in a simple shearing flow bears some resemblance to the diffusion of Brownian particles (Rallison & Hinch 1986). To determine the diffusivities for Brownian particles, one actually follows a particular (tracer) particle that is initially located at the origin and determine its displacement, r, as a function of time, t. Repeating this process for many different starting conditions allows the construction of the mean-square displacement $\langle r^2(t)\rangle$.

As a particle moves from some initial position in a homogeneous suspension, it interacts hydrodynamically with its neighbours. For short times, the test particle sees an isotropic cage surrounding it, which affects its motion only in modifying the mean hydrodynamic resistance. Its motion is diffusive in character with $\langle r^2(t)\rangle \sim t$. This purely diffusive motion persists as long as the configuration of particles surrounding the test particle is not influenced significantly by the motion of this test particle. The particle motion can be described through a short-time self-diffusion coefficient, D_0^s,

$$\langle r^2(t)\rangle \sim D_0^s\, t. \tag{1.1}$$

Equation (1.1) holds for times over which the relative positions of the particles surrounding the test particle hardly change. As time progresses, the test particle interacts with its neighbours and its motion cannot be described by a pure diffusion process, that is, $\langle r^2(t)\rangle/t \neq$ constant. Over a very long time period the test particle encounters many other particles. The sum of these random steps can again be considered as a diffusion process with a long-time self-diffusion coefficient, D_∞^s,

$$\langle r^2(t)\rangle \sim D_\infty^s\, t. \tag{1.2}$$

Equation (1.2) holds for 'long times' during which the test particle moves, on average, a distance equal to many particle diameters.

Bossis & Brady (1987) have used Stokesian dynamics to predict the self-diffusion of monodispersed suspensions of Brownian spheres ($Pe = 0$–1000) including hydrodynamic interactions. For such particles, if the mobilities of the spheres are known – as a function of their positions – D_0^s is calculated using a generalized Einstein relation (Batchelor 1976). This relates D_0^s to an average of these mobilities over all the configurations of the spheres. Beenakker & Mazur (1984) presented a theory for the concentration dependence of D_0^s, which is valid up to high concentrations, that accounts for many-body hydrodynamic interactions. They obtained a second-order virial expansion in ϕ_v for Brownian particles. Experimentally, D_0^s has been determined for Brownian particles using dynamic light-scattering techniques (Fijnant 1981; Pusey & Van Megen 1983; Ottewill & Williams 1987). Phillips, Brady & Bossis (1988) determined D_0^s numerically for hard-sphere dispersions using a Monte Carlo technique combined with Stokesian dynamics. Their results agree with both the experiments and theories for Brownian particles mentioned above. For suspensions with purely hydrodynamic interactions among spheres, D_0^s is the average mobility of a particle and can be calculated by averaging the mobilities over many sphere configurations. However, except for the value of D_0^s calculated by Bossis & Brady (1987) for a monolayer of spherical particles with purely hydrodynamic interactions, at an area fraction, ϕ_a, of 0.453 there are no other results for D_0^s for large sphere suspensions.

The long-time diffusivity for suspensions with purely hydrodynamic interactions among spheres, D_∞^s, has been experimentally determined for monodispersed suspensions by Leighton & Acrivos (1987*a*) using a circular Couette device of the type originally used by Eckstein *et al.* (1977). The outer cylinder was rotated and the motion of a tracer sphere was observed. Measurements were made of the successive transit times required for a tagged sphere to complete full 360° orbits about the cylinder axes. Leighton & Acrivos (1987*a*) derived an expression for the probability density, $p(t' \mid t)$, of completing the second orbit in time interval t', given that the first transit required time t. On this basis they were able to devise a scheme that permitted the calculation of D_∞^s solely from their transit time measurements. This represented a simplification over the original measurements made by Eckstein *et al.* (1977), whose determinations of D_∞^s had required measurement of the radial location of the tagged sphere after each completed orbit, as well as the transit time.

For a dilute suspension of monodispersed spherical particles of radius a, Leighton & Acrivos (1987*a*) found D_∞^s to have the asymptotic form $0.5\dot{\gamma}a^2\phi_v^2$. This is in contrast to the linear dependence of D_∞^s upon ϕ_v that was reported in the same limit by Eckstein *et al.* (1977). Leighton & Acrivos (1987*a*) also provided measurements of D_∞^s for solid concentrations up to $\phi_v = 0.40$. We note that both Eckstein *et al.* (1977) and Leighton & Acrivos (1987*a*) neglect the bounding walls of the Couette device, as well as its curvature, in order to simplify their analyses. An alternative theoretical approach, which is essentially similar to the Taylor–Aris-type dispersion analysis, was presented by Nadim (1988). It provided a foundation for more accurate measurements of D^s_∞, particularly for concentrated suspensions where D^s_∞ is large and the marked particle quickly diffuses to the vicinity of the walls. Full account was taken of the curvature of the Couette device geometry and of the excluded volume effect resulting from the finite size of the tagged sphere that prevents its centre from approaching the bounding walls beyond one particle radius.

More recently, Phan & Leighton (1993) have extended the work of Leighton & Acrivos (1987*a*) and measured the shear-induced tracer diffusivity in a concentrated suspension (0.3–0.55 solids volume fraction) of non-colloidal spheres (670 μm average diameter) by examining the random walk of marked particles with diameters ranging from 213 to 6350 μm. For measurements in the plane of shear Phan & Leighton followed the approach of Leighton & Acrivos (1987*a*) and examined the influence of the walls through Monte Carlo simulation of the migration process, which showed the transition from the unbounded limit to the bounded Taylor dispersion limit studied by Nadim (1988). Measurements normal to the plane of shear were made by directly observing the random motion of the tracer particle normal to the plane of shear in digitized video images. Both diffusivities were found to scale as $\dot{\gamma}a_s^3/a_t$, where a_s is the suspending particle radius and a_t is the tracer particle radius, for $a_s/a_t \geqslant 2$. The diffusivity in the plane of shear appeared to approach a constant value for $a_s/a_t \leqslant 1$. Phan & Leighton also found that, in contrast to the shear-induced diffusivity which results from particles being pushed from regions of high concentration to low and diverges at high concentrations in a manner similar to the suspension viscosity, the tracer diffusivity appeared to approach a constant value at high concentrations, and the tracer diffusivity normal to the plane of shear was approximately two-thirds of that in the plane for all concentrations and tracer particle sizes.

All of the results mentioned above (except for Phan & Leighton 1993, whose tracer particles had different sizes as compared with the suspending spheres), both for D^s_0 and D^s_∞, are for monodispersed suspensions only. Suspensions of practical interest are rarely composed of uniform sized spheres. At high concentrations, processing properties, specifically viscosity, are more favourable if bimodally distributed suspensions are used (e.g. Chong, Christiansen & Baer 1971; Miller *et al.* 1991). Recently, we have used Stokesian dynamics to calculate the macroscopic rheological properties of bimodal suspensions of spherical particles (Chang & Powell 1993). In this paper, we address the issues of the influence of variations in particle size on the shear-induced diffusive transport. We present results for both the microstructure (e.g. pair-connectedness function) and the average mobilities and long-time self-diffusion coefficients for bimodal suspensions as determined by Stokesian dynamics. In §2 we give a brief description of Stokesian dynamics as used to simulate suspensions of bimodally distributed spherical particles in a Newtonian fluid. The appropriate averages defining the average mobility (i.e. D^s_0 for $Pe = \infty$) and the long-time self-diffusion coefficient are presented. In §3 we present simulation results for a monolayer of unequal-sized spheres subjected to a simple shearing flow. Section 4 provides a brief synopsis of the principal results.

2. Simulation method

2.1. *Stokesian dynamics*

A discussion of the application of Stokesian dynamics to suspensions of unequal-sized spheres is given in Chang & Powell (1993). Formulae required to implement this technique can be found in Chang (1993). Here, we provide a brief review of those results. We consider a finite system of particles consisting of two sets of rigid spheres having different radii a and b. The particles are small enough such that the particle Reynolds numbers, Ua/ν and Ub/ν, are much less than unity where U is a characteristic velocity and ν is the kinematic viscosity of the fluid. There exists a set of linear relations between the rigid-body motion of the spheres and the moments (forces, torques, stresslets) exerted on the particles. For the *resistance problem*, the moments on the spheres are determined for specified translational and rotational velocities of the particles in an ambient linear velocity field. using the grand resistance matrix, $\boldsymbol{R}$, the force and torque ($\boldsymbol{F}$) and the stresslet ($\boldsymbol{S}$) exerted by the particles on the fluid are related to the particle translational and rotational velocities ($\boldsymbol{U}$) and the rate of strain of the undisturbed flow, $\boldsymbol{E}^{\infty}$, through

$$\begin{pmatrix} \boldsymbol{F} \\ \boldsymbol{S} \end{pmatrix} = \boldsymbol{R} \begin{pmatrix} \boldsymbol{U}-\boldsymbol{U}^{\infty} \\ -\boldsymbol{E}^{\infty} \end{pmatrix}, \tag{2.1}$$

$$\boldsymbol{R} = \begin{pmatrix} \boldsymbol{R}_{FU} & \boldsymbol{R}_{FE} \\ \boldsymbol{R}_{SU} & \boldsymbol{R}_{SE} \end{pmatrix}. \tag{2.2}$$

For example, for N particles, $\boldsymbol{U}-\boldsymbol{U}^{\infty}$ is a vector of dimension $6N$ containing the translational and rotational velocities of all N particles relative to the imposed flow at infinity, $\boldsymbol{U}^{\infty}$, evaluated at the centre of the particles; $\boldsymbol{E}^{\infty}$ is a vector of dimension $5N$ that repeats the imposed rate of strain for each particle; $\boldsymbol{F}$ is a $6N$ vector containing the force and torque exerted by the particles on the fluid; and $\boldsymbol{S}$ has dimension $5N$ and contains the particle stresslets (the symmetric and traceless part of the first moment of the force distribution integrated over the particle surfaces, or physically, the contribution to the bulk stress due to the existence of the particles). The inverse of the grand resistance matrix, the grand mobility matrix, $\boldsymbol{M}$ allows $\boldsymbol{U}$ to be calculated from the applied moments

$$\begin{pmatrix} \boldsymbol{U}-\boldsymbol{U}^{\infty} \\ -\boldsymbol{E}^{\infty} \end{pmatrix} = \begin{pmatrix} \boldsymbol{M}_{UF} & \boldsymbol{M}_{US} \\ \boldsymbol{M}_{EF} & \boldsymbol{M}_{ES} \end{pmatrix} \cdot \begin{pmatrix} \boldsymbol{F} \\ \boldsymbol{S} \end{pmatrix}. \tag{2.3}$$

When only two spheres are considered, the grand resistance matrix is known exactly for all centre–centre separations and all sphere size ratios (Jeffrey & Onishi 1984; Kim & Karrila 1991; Jeffrey 1992). Similarly, the grand mobility matrix (Chang 1993; Chang & Powell 1994*b*) can be found using the results of Jeffrey & Onishi (1984) and Kim & Karrila (1991). The analysis of concentrated suspensions requires the calculation of many-body hydrodynamic interactions among the spheres. Results for pairs of particles are not sufficient in studies of concentrated suspensions, where the hydrodynamic interactions are not pair-wise additive (Glendinning & Russel 1982). Recently, Brady, Bossis and coworkers (Bossis & Brady 1984, 1987, 1989; Brady & Bossis 1985, 1988; Durlofsky, Brady & Bossis 1987; Durlofsky & Brady 1989; Brady *et al.* 1988) have developed a simulation technique for treating many-body interactions of concentrated suspensions which is termed 'Stokesian dynamics'. This uses a molecular-dynamics approach to follow the time evolution of the positions of particles in a suspension, from which mean field microstructural information such as the pair-correlation functions can be derived. Macroscopic transport properties, such as shear viscosity, can also be calculated using appropriate averaging schemes (Brady & Bossis 1988).

Stokesian dynamics, also termed the multipole-moment method (Weinbaum, Ganatos & Yan 1990), deals with the hydrodynamic interactions among spheres in concentrated suspensions in two ways. Firstly, the grand mobility matrix is inverted to obtain the grand resistance tensor, which describes the far-field many-body interactions. The grand mobility matrix only describes the velocity disturbance produced by a few lowest-order multipoles representing each sphere, and does not contain the reflections of the other spheres required to describe the screening effects associated with many-body interactions. However, its inversion produces the grand resistance matrix, in which sums of all the multipole reflections of the lowest order multipoles are included. To form the grand mobility matrix for bimodal suspensions, we take the integral solution of the Stokes equation and use the multipole-moment method to expand the force density on the surface of each particle. The zeroth moment is the total force, and the first moment has both antisymmetric and symmetric parts (the torque and stresslet, respectively). We truncate the multipole expansion after the dipole terms, although two higher multipole contributions that result from the finite size of the sphere are included (Chang & Powell 1993, 1994*b*). The grand mobility matrix is then readily constructed using Faxén's laws (Batchelor & Green 1972).

While the multipole expansion is truncated after the dipole terms, inverting the mobility matrix solves the many-body problem at the level of forces, torques, and stresslets. This many-body approximation to the resistance matrix lacks an accurate representation of the hydrodynamic forces between nearly touching particles. This would be reproduced upon inversion of the mobility matrix if all multipole moments were included, which is impractical. This gives rise to the second essential feature of Stokesian dynamics: the inclusion of near-field lubrication effects between particles using exact formulae for two-body interactions. Owing to their short-range nature, such lubrication forces can be introduced in a pairwise-additive fashion in the resistance matrix. The grand resistance matrix can then be partitioned as in (2.2) and used to write the evolution equation

$$U-U^{\infty} = \boldsymbol{R}_{FU}^{-1}\cdot(F+\boldsymbol{R}_{FE}\cdot\boldsymbol{E}^{\infty}). \tag{2.4}$$

Equation (2.4) permits the velocities U to be found for an imposed linear flow at a given (instantaneous) particle configuration. Once the velocities of the spheres are found, the new particle positions are calculated with a given time step. Typically, this is done by using regular predictor or predictor-corrector methods (Carnahan, Luther & Wilkes 1969).

The macroscopic properties of the suspension are found from appropriate definitions that involve averages over particle configurations and, in a dynamic simulation, over time. For example, the N-particle diffusion tensor, $\boldsymbol{D}$, is defined by (Brady & Bossis 1988)

$$\boldsymbol{D} \equiv kT\boldsymbol{R}_{FU}^{-1} = kT\boldsymbol{M}, \tag{2.5}$$

where k is the Boltzmann constant, and T is the absolute temperature. The average mobility at $Pe=\infty$ is obtained from $\boldsymbol{D}$ by

$$D_0^s = \langle D_{ii}\rangle, \tag{2.6}$$

where $\langle\cdot\rangle$ denotes an average over all configurations and the subscript ii (no sum on i) indicates that only the diagonal, or self, terms are included in the averaging. The long-time self-diffusivity D^s_∞, which measures the ability of a particle to wander far from its starting point, is defined through (Brady & Bossis 1988; Bossis & Brady 1990)

$$D^s_\infty = \lim_{t\to\infty} \frac{1}{2}\frac{\mathrm{d}}{\mathrm{d}t}\langle (x-\langle x\rangle)^2\rangle. \tag{2.7}$$

Here, $\langle (x-\langle x\rangle)^2\rangle$ is the mean-square displacement of a reference particle.

2.2. *Simulation of a sheared monolayer*

For the full three-dimensional problem, there are three unknown velocities (or forces), three angular velocities (or torques) and five strain rates (or stresslets) for every particle. The grand mobility tensor is therefore of size $11N \times 11N$, the inversion of which requires $O((11N)^3)$ operations. For a system with 50 or more particles, this is too computationally intensive for dynamic simulations. To reduce the computational cost, we have performed simulations of a monolayer of unequal-sized (bimodal) rigid non-Brownian, and non-colloidal spherical particles subjected to a simple shearing flow. In a monolayer the centres of the spherical particles are required to lie in the same plane, the plane of shear, which results in substantial computational savings (the number of degrees of freedom per particle is reduced from 11 to 6) without compromising the essential physics. Particle–particle interactions which result from the macroscopically imposed simple shearing flow, having a shear rate $\dot{\gamma}$, all occur in this plane. The bulk rate-of-strain tensor $\boldsymbol{E}^\infty$ is given by

$$\boldsymbol{E}^\infty = \frac{\dot{\gamma}}{2}\begin{bmatrix} 0 & 1 & 0 \\ 1 & 0 & 0 \\ 0 & 0 & 0 \end{bmatrix} \tag{2.8}$$

and the bulk vorticity $\boldsymbol{\Omega}$ is

$$\boldsymbol{\Omega} = -\tfrac{1}{2}\dot{\gamma}(0,0,1). \tag{2.9}$$

Creeping flow conditions apply and the particles are assumed to be neutrally buoyant. There are neither external forces (e.g. due to gravity) nor external torques (e.g. due to a magnetic field) acting on the particles. We model an infinite suspension by replicating a basic unit cell using periodic boundary conditions. Each particle is centred on its own periodic cell and interacts only with its neighbours in that cell. For a suspension monolayer, Ewald sums that account for long-range effects, are not required since the particle interactions are convergent for force-free and torque-free particles (Bossis & Brady 1990). Generally, it can be shown (Bossis & Brady 1984; Brady & Bossis 1985) that the hydrodynamic interactions are long-ranged, falling off as the inverse square of the distance between the centres of spheres for force-free particles. Particles outside the periodic cell make no contribution to the translational–rotational velocity of the particle at the centre of the periodic cell to within an error $O(R^{-2})$, R being a characteristic dimension of the cell. In our case, R is the cell length, H, non-dimensionalized by the radius of a large sphere. Thus, as the size of the periodic cell increases, the effect of the particles outside the cell can be made arbitrarily small. This is achieved by choosing N, the total number of particles, appropriately once the size ratio of the spheres, λ, and the areal fraction of total solids that are small spheres, ξ, are fixed. Usually, we choose the magnitude of $O(R^{-2})$ as 0.01. To check the effect of the total number of particles and the size of the periodic cell, we have tested two different conditions for each λ with ξ fixed but changing N and H. For example, this is shown in table 1 for $\lambda = 2$, $\xi = 0.273$ with $N = 25$ or 49. The magnitude of $O(R^{-2})$ errors for these two cases is 0.012 and 0.006, respectively. We obtained statistically the same results for the average mobilities and long-time diffusivities for these two cases. This shows that within the error of 0.01 the influence of N and H is

λ	ξ	N_l	N_s
2	0.073	19	6
2	0.273	10	15
2	—	20	29
2	0.494	10	39
2	0.642	6	43
2	0.836	3	61
4	0.074	11	14
—	—	22	27
4	0.273	7	42
4	0.495	6	94

TABLE 1. Parameters for simulations. Two types of numerical experiments were performed: (i) (see above) fix the size ratio of spheres, λ, at 2 or 4 and the area fraction of solids, ϕ_a, at 0.503, then vary the fraction of small spheres, ξ; (ii) set $\xi = 0.27$ and for seven values of ϕ_a (0.118, 0.236, 0.354, 0.453, 0.503, 0.55, 0.60) determine the effect of varying the size ratio of spheres from $\lambda = 1$ to $\lambda = 4$.

limited. The same scenario is also found for $\lambda = 4$, $\xi = 0.074$ with $N = 25$ or 49, where the magnitude of $O(R^{-2})$ errors is 0.013 and 0.007, respectively.

The simulations were initiated with the particles located at random positions in the periodic cell. Upon starting the shearing flow microstructural changes were calculated in time until steady state was reached. This was determined by monitoring the time average of the square of the x- and y-components of the particle velocities relative to the bulk shear flow. We note that while steady state was achieved on a time-average basis, small fluctuations occurred on the short-time scale. We used a shear rate of 1.0. With a time step of 2×10^{-4}, steady state was reached in approximately 100000 time steps. The pair-connectedness function (Seaton & Glandt 1987), $p(r)$, which is a measure of suspension microstructure and defined in §3, and average mobilities at $Pe = \infty$, D_0^s, reported below were averaged over the last 100000 time steps. The long-time diffusivity, D_∞^s, was calculated using the results for the whole time period. To determine the statistical errors, simulations for the same values of solid area fraction ϕ_a, λ, ξ and N were performed starting from different initial conditions, for a total of five numerical experiments for each suspension. We report results for areal fractions up to 0.6. Simulations of more concentrated suspensions become too expensive, as the time step must be reduced to follow the particle trajectories without particles overlapping during a time step. All calculations were performed in double precision on an IBM 3090, DEC 5000/200, or a Cray Y-MP. A summary of the different runs is presented in table 1, which gives the values of the parameters λ, ξ and ϕ_a as well as the number of large and small spheres, N_1 and N_s respectively.

3. Results and discussion

In this section we present dynamic simulation results for both microstructure (pair-connectedness function) and macroscopic rheological properties (average mobility and long-time self-diffusivity) of bimodal suspensions. All simulations were started at $t = 0$ with the particles located randomly in the periodic cell. The initial positions were determined by first placing the spheres in a regular array and then perturbing them a small random distance. The only constraint placed on the random displacements was that they not be so large as to cause particles to overlap. A typical initial configuration for a bimodal suspension having $\phi_a = 0.50$, $\xi = 0.27$ and $\lambda = 2$ is shown in figure 1(a). Once a stationary state has been reached, the suspension is, on average, organized

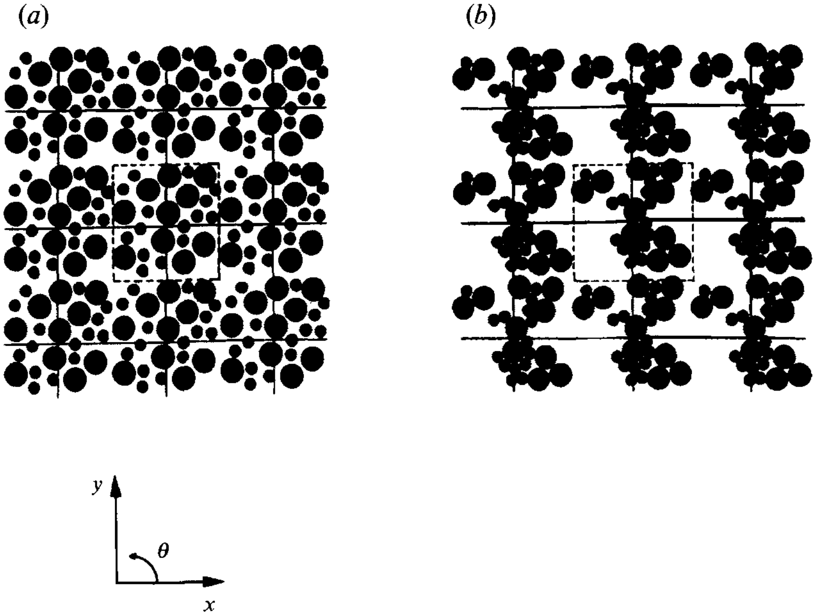

FIGURE 1. (*a*) Initial configuration for a randomly distributed bimodal suspension, with $\phi_a = 0.50$, $\xi = 0.27$ and $\lambda = 2$. The dashed lines are the boundaries of the periodic cell. (*b*) Instantaneous microstructure after steady state is reached. Small spheres tend to fit in the spaces among the large spheres with the particles forming clusters.

according to the relative locations of the small and large particles. An instantaneous 'snapshot' of the suspension microstructure is depicted in figure 1(*b*). We observe that small spheres tend to fit in the spaces among the large spheres with the particles forming clusters. A series of animated 'movies' generated from simulation results for both monodispersed and bimodal suspensions with different λ and ξ have shown that these clusters tend to form along the compressive flow direction (135°) rotate as a solid rod (due to vorticity) and then break up in the extensional flow direction (45°) (Chang & Powell 1993). Similar results for monodispersed suspensions have also been reported by Brady & Bossis (1988).

While observations such as these provide good qualitative insight into the dynamics of suspensions, quantitative features of the suspension microstructure must be determined in order to macroscopically model transport properties. The microstructure itself can be described through one of various measures (pair-distribution or pair-connectedness function) of the average relative positions of particles. The transport properties are usually described through the relative viscosity (Chang & Powell 1993) and the diffusivities. The diffusivities give average measures of the motions of individual particles. Hence, combining distribution functions with the diffusivities gives the instantaneous microstructure as well as macroscopic transport properties of a suspension.

3.1. *Pair-connectedness function* $p(r)$

One way to describe the microstructure of a suspension is through the particle distribution functions. There are different distribution functions that provide microstructural information and measures of clustering in continuum-percolation systems. For example, the pair-distribution function, $g(r)$ (Bossis & Brady 1984; Chang & Powell 1993), has been defined as the probability of finding a particle centre at position r given that there is a particle centre at the origin $r = 0$, divided by the number

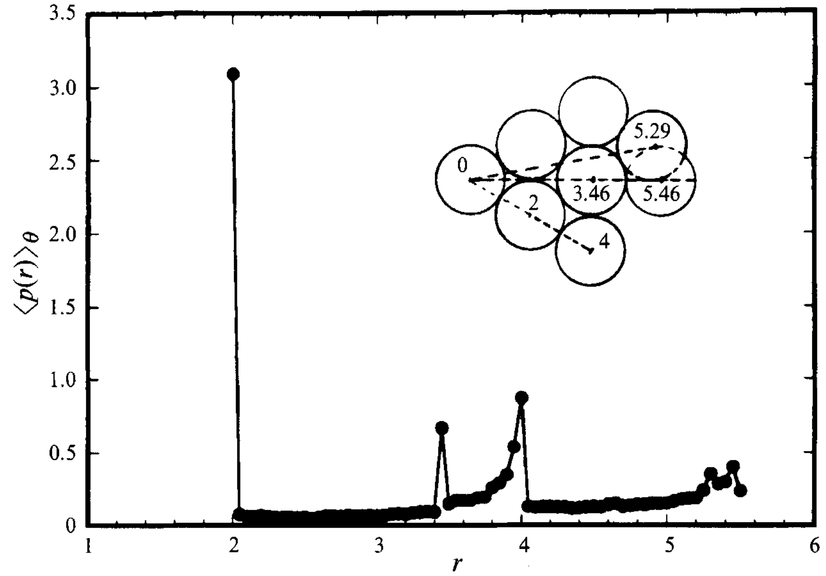

FIGURE 2. The radial dependence of the angle-averaged pair-connectedness function $\langle p(r)\rangle_\theta$ for a monodispersed suspension, $\lambda = 1$, having $\phi_a = 0.50$ and $N = 49$. The dimensionless sphere diameter is 2.

density. In sheared suspensions $g(\mathbf{r})$ is generally both angularly and radially dependent, for example in two-dimensions $g(\mathbf{r}) = g(r, \theta)$. In our companion paper (Chang & Powell 1993), we have presented results for the angle-averaged pair-distribution function, $\langle g(r)\rangle_\theta$, for bimodal suspensions with the size ratio of the spheres $\lambda = 2$ and 4, the area fraction of small spheres of total solids being 0.27, and the area fraction of total solids being 0.5. These indicated that in concentrated suspensions nearly 'touching' particle pairs (large–large, large–small, or small–small spheres) form due to the lubrication forces between them. The pair-connectedness function, $p(\mathbf{r}_i, \mathbf{r}_j)$, provides another measure of suspension microstructure. It is of central importance in describing particle distributions when considering the statistical mechanics of clustering in continuum systems (Seaton & Glandt 1987; Sevick, Monson & Ottino 1988; Lee & Torquato 1988; Kim & Torquato 1990).

The pair-connectedness function is defined such that the quantity $n^2 p(\mathbf{r}_i, \mathbf{r}_j)\, \mathrm{d}\mathbf{r}_i\, \mathrm{d}\mathbf{r}_j$ represents the probability that two particles i and j reside in volume elements $\mathrm{d}\mathbf{r}_i$ and $\mathrm{d}\mathbf{r}_j$ centred at $\mathbf{r}_i$ and $\mathbf{r}_j$ respectively, and are members of the same cluster, with n being the number density of particles in the system. For a suspension monolayer undergoing simple shearing flow, the pair-connectedness function is both angularly and radially dependent. It differs from the pair distribution function, $g(\mathbf{r})$, in that for $p(\mathbf{r})$ the particle pairs must belong to the same cluster. Thus, $p(\mathbf{r})$ provides direct information about the particle microstructure within clusters. To compute $p(\mathbf{r})$ as well as other measures of cluster size, we must distinguish between different clusters. This is achieved by specifying the maximum particle–particle separation required for two (or more) particles to be a cluster. For bimodal suspensions, two particles of radius a and b are 'directly' connected if the gap, ϵ, between two spheres satisfies the relation

$$\epsilon/(a+b) \ll 1. \tag{3.1}$$

For the results presented here, we have followed Bossis & Brady (1989) and chosen ϵ as 10^{-2} for the separation (or maximum 'bond') distance which defines that two

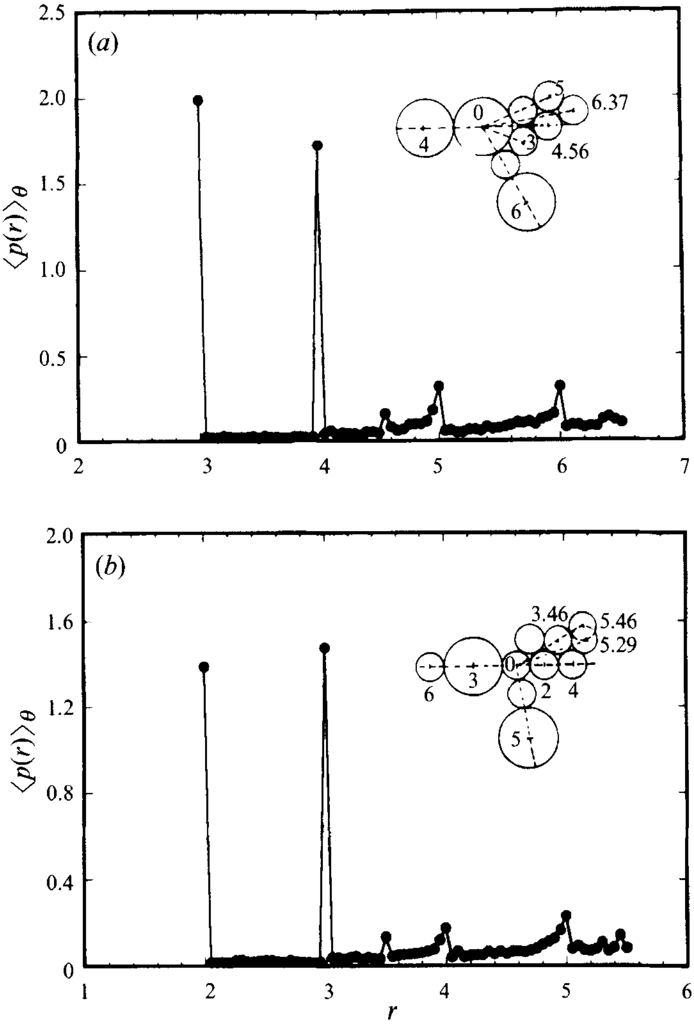

FIGURE 3. The radial dependence of the angle-averaged pair-connectedness function $\langle p(r) \rangle_\theta$ for bimodal suspensions with $\lambda = 2$, $\phi_a = 0.50$ and $\xi = 0.27$. (*a*) $\langle p(r) \rangle_\theta$ relative to a large sphere; (*b*) $\langle p(r) \rangle_\theta$ relative to a small sphere.

spheres belong to the same cluster. The results for $\epsilon = 10^{-1}$ and 10^{-3} are close to those for $\epsilon = 10^{-2}$. For example, for the case of $\lambda = 1$ and $\phi_a = 0.50$, the number-average mean cluster size is 6.2 for $\epsilon = 10^{-2}$ as compared with 6.4 and 6.1 for $\epsilon = 10^{-1}$ and 10^{-3} respectively.

Pairs of particles can be 'indirectly' connected through chains of the other particles. In order to distinguish different clusters in the suspension we employ a cluster-counting algorithm, similar to the 'cluster-labelling' method that was originally developed for lattice percolation (Hoshen & Kopelman 1976) and subsequently adapted for continuum percolation (Gawlinski & Stanley 1981). The essence of the algorithm is to give each particle a number that indexes it within the total particle population (1 to N) and a label that denotes the cluster of which it is a member. As an example, the label of particle number 1 is '1'. If no bonds emanate from it, it is a single particle 'cluster' with size 1. If bonds emanate from this particle, the algorithm moves along each of them to the neighbouring particles and assigns to the 'attached' particles the label '1'.

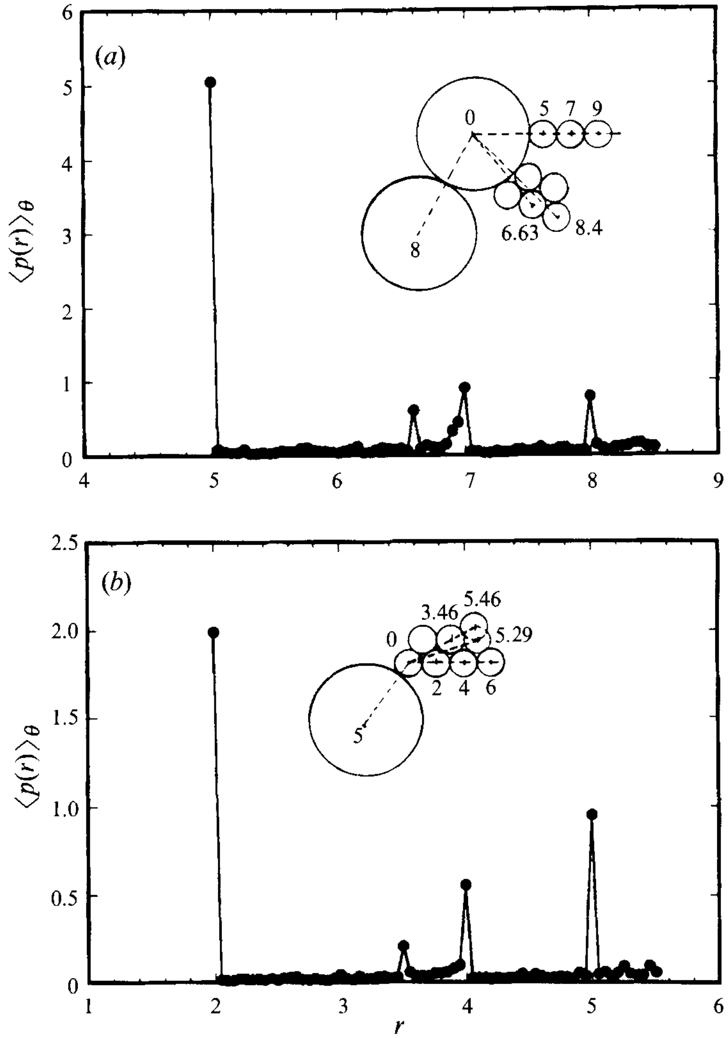

FIGURE 4. As figure 3 but with $\lambda = 4$. (*a*) $\langle p(r)\rangle_\theta$ relative to a large sphere; (*b*) $\langle p(r)\rangle_\theta$ relative to a small sphere.

The algorithm moves systematically from particle to particle, assigning labels in this way until all the bonds that are accessible starting at particle 1 are traversed. When no bonds remain to be traversed, all the particles attached either directly or indirectly (i.e. via other particles) to particle 1 are labelled. If particle number 2 already has a label, it is not considered again. If it does not have a label, it and all the particles connected to it are given the label 2. This procedure is repeated for each of the $N(=N_l+N_s)$ particles. Upon completion, each particle has a label denoting the cluster to which it belongs and the cluster size, pair-connectedness function as well as other statistic measures for a particular configuration can be calculated.

Our simulations use periodic boundary conditions to simulate a suspension of 'infinite' extent. For the simple shearing flow represented by (2.8) and (2.9), the periodic conditions in the x- and z-directions are straightforward, but periodicity in y requires a translation in x by an amount $H\dot{\gamma}t$ in order to preserve the bulk linear shearing flow (Evans 1979; Bossis & Brady 1984). Here, H is the periodic box height

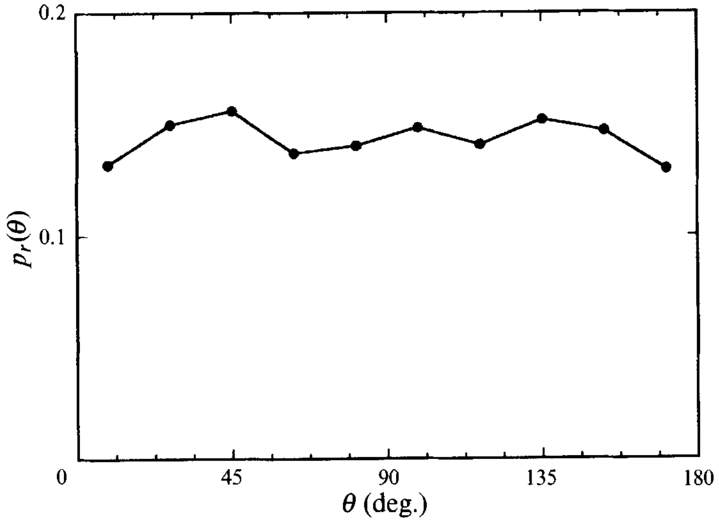

FIGURE 5. The angular dependence of the pair-connectedness function $p_{\Delta r}(\theta)$ in the Δr range $2 \leqslant r \leqslant 2.05$ for monodispersed suspensions having $\phi_a = 0.50$. The symmetry of $p_{\Delta r}(\theta)$ about $\theta = 90°$ implies that there are no normal-stress differences, with purely hydrodynamic interactions among particles.

in the y-direction. While the central cell is surrounded by identical replicas in the x-direction, this is neither necessarily nor usually the case in the y-direction. In calculating $p(\boldsymbol{r})$, the relationship between a reference particle and its nearest $N-1$ neighbours is considered. Some of the neighbours might not be in the same central cell as the reference particle. Just as the record of the bonding between particle accounts for bonding between particles in different replicas, the procedure to determine $p(\boldsymbol{r})$ correctly finds the cluster size distribution in the infinite system of a suspension.

The computation of the angle-averaged pair-connectedness function, $\langle p(r)\rangle_\theta$, is now relatively straightforward. First, we construct concentric shells of radii $r_m = m\Delta r$, where $m = 1, 2, 3, \ldots, M$ and $M\Delta r \leqslant H\sqrt{2}$, around each particle in the system, where Δr is a distance which is small compared to a and b. We have used $\Delta r = 0.05$, with Δr being non-dimensionalized by the radius of the small sphere. We count the number of particles whose centres lie in a specific shell and are connected (directly or indirectly) to the central reference particle. The number of connected particles for each value of m is obtained from which $\langle p(r)\rangle_\theta$ is constructed. Figure 2 shows $\langle p(r)\rangle_\theta$ for a monodispersed suspension, $\lambda = 1$, with 49 spheres and $\phi_a = 0.50$. Here, it is seen that a reference sphere of dimensionless radius 1 has the highest probability of finding other spheres as its nearest neighbours (the first peak) and has a lower probability of finding doublets (third peak) and triplets (cyclic form, second peak) next to it. We have shown in Chang & Powell (1993) that there was no second peak ($r \approx 3.46$) for $\phi_a = 0.4$. As the concentration is increased, the cyclic conformation is favoured as the less compact linear trimers are more likely to be absorbed into larger clusters. The small peaks at $r \approx 5.29$ and 5.46 are due to the cluster structures shown in the sketch.

Figures 3 and 4 show $\langle p(r)\rangle_\theta$ for bimodal suspensions with the same $\phi_a = 0.50$ and $\xi = 0.27$, but different λ, 2 and 4 respectively. For the $\lambda = 2$ case shown in figure 3 we have used 20 large spheres and 29 small spheres in the simulations. Figure 3(a) shows $\langle p(r)\rangle_\theta$ for a large sphere (radius 2) centred at $r = 0$. Such a large sphere is observed to have a higher probability of finding small spheres as its nearest neighbours (the first peak) than other large spheres (the second peak). We also see that some small–small

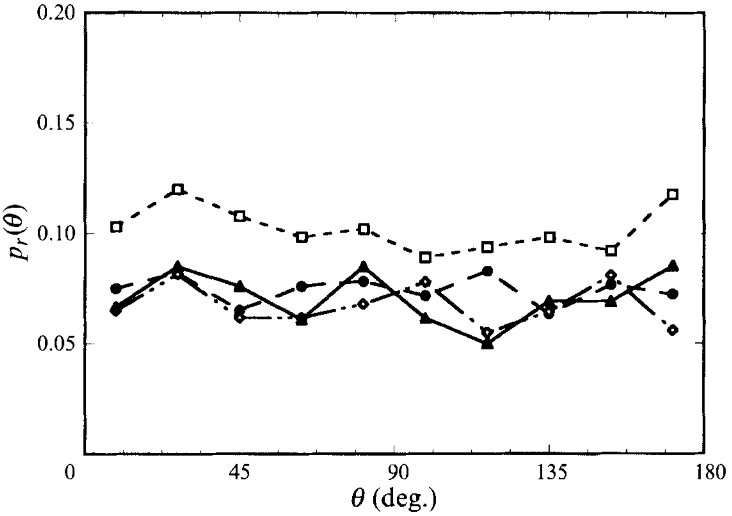

FIGURE 6. The angular dependence of the pair-connectedness function near contact $p_{\Delta r}(\theta)$ for bimodal suspensions with $\lambda = 2$, $\phi_a = 0.50$ and $\xi = 0.27$. The Δr ranges for the large sphere are $3 \leqslant r \leqslant 3.05$ and $4 \leqslant r \leqslant 4.05$; for the small sphere the ranges are $2 \leqslant r \leqslant 2.05$ and $3 \leqslant r \leqslant 3.05$. □, $3 \leqslant r \leqslant 3.05$ (large sphere); ●, $4 \leqslant r \leqslant 4.05$ (large sphere); ◇, $2 \leqslant r \leqslant 2.05$ (small sphere); ▲, $3 \leqslant r \leqslant 3.05$ (small sphere).

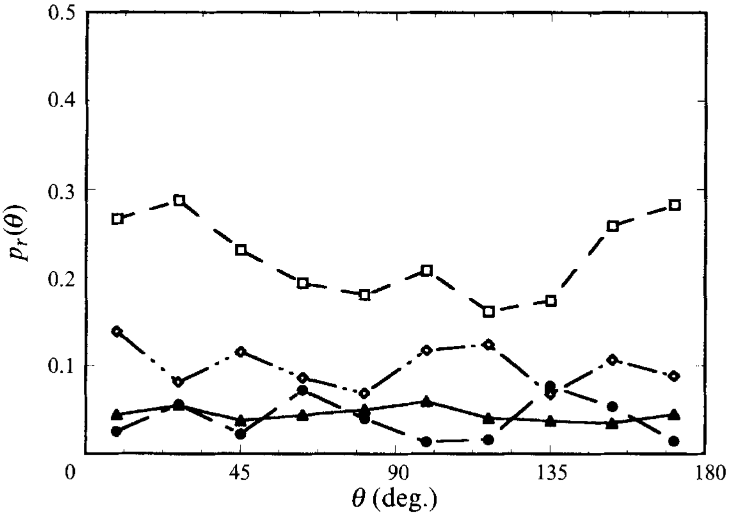

FIGURE 7. The angular dependence of the pair-connectedness function near contact $p_{\Delta r}(\theta)$ for bimodal suspensions with $\lambda = 4$, $\phi_a = 0.50$ and $\xi = 0.27$. The Δr ranges for the large sphere are $5 \leqslant r \leqslant 5.05$ and $8 \leqslant r \leqslant 8.05$; for the small sphere the ranges are $2 \leqslant r \leqslant 2.05$ and $5 \leqslant r \leqslant 5.05$. □, $5 \leqslant r \leqslant 5.05$ (large sphere); ●, $8 \leqslant r \leqslant 8.05$ (large sphere); ◇, $2 \leqslant r \leqslant 2.05$ (small sphere); ▲, $5 \leqslant r \leqslant 5.05$ (small sphere).

(peak at $r \approx 5$) and small–large (peak at $r \approx 6$) sphere doublets next to the large reference particle form linear arrays of particles. The small peak at $r \approx 4.5$ indicates that a large reference sphere is 'touching' a cyclic trimer of small spheres. The small peak at $r \approx 6.37$ is from the cluster structure in the sketch. Figure 3(*b*) shows $\langle p(r) \rangle_\theta$ for a small sphere (radius 1) centred at $r = 0$. Here, it is seen that there is a slightly higher probability of finding large spheres as its nearest neighbours than small spheres. Peaks at $r \approx 3.5$ and 4.0 result from the same cluster morphology described in figure

2: cyclic trimers and doublet of small spheres next to the reference small sphere, respectively. Small–large sphere doublets next to the reference small sphere give rise to the peak at $r \approx 5.0$. The small peaks at $r \approx 5.29$ and 5.46 also result from the same cluster morphology described in figure 2 and due to the cluster structures shown in the sketch.

For the case of $\lambda = 4$, 7 large spheres and 42 small spheres were used. Since there are many more small spheres than large spheres in the suspension, one expects that both large and small spheres have higher probabilities of finding small spheres as their nearest neighbours rather than large spheres. Figure 4 supports this hypothesis. The large peak in figure 4(*a*) at $r \approx 5$ represents the centre of a small sphere next to a large sphere of radius 4. This is much larger than the peak at $r \approx 8$, which results from large-sphere doublets. In figure 4(*b*) the peak at $r \approx 2$ results from small-sphere doublets, which are more probable than small sphere–large sphere doublets (peak at $r \approx 5$). The peak at $r \approx 7.0$ in figure 4(*a*) indicates that small–small sphere doublets were formed next to the reference large sphere, and the peak at $r \approx 6.6$ shows that a large sphere is 'touching' a cyclic trimer of small spheres. The small peak at $r \approx 8.42$ is due to the cluster structure shown in the sketch. In figure 4(*b*), the peaks at $r \approx 3.5$ and 4.0, and small peaks at $r \approx 5.29$ and 5.46 have the same structures as those described above for figures 2 and 3(*b*). In our earlier findings (Chang & Powell 1993), we did not have the small peaks at $r \approx 4.5$ in figure 3(*a*), $r \approx 3.5$ in figure 3(*b*), $r \approx 6.5$ in figure 4(*a*) and $r \approx 3.5$ in figure 4(*b*). The reason might be the method used to calculate $\langle g(r) \rangle_\theta$ in Chang & Powell (1993) where only four different angles, 9°, 27°, 99° and 171°, were used. In calculating $\langle p(r) \rangle_\theta$ we have used the full 360°.

Figure 5–7 illustrate the angular dependence of the pair-connectedness function near contact, $p_{\Delta r}(\theta)$, for $\Delta r = 0.05$. Upstream of the reference particle is represented by $\theta = 180°$, while $\theta = 0°$ is the downstream direction, where θ is shown in figure 1. The conditions of the simulations in figures 5–7 are equivalent to those of figures 2–4, respectively. For monodispersed suspensions, figure 5, we have used $2 < r < 2.05$, which includes the first-nearest-neighbour peak. For $\lambda = 2$, figure 6, we have used two different sets of ranges for each size of sphere, i.e. $3 < r < 3.05$ and $4 < r < 4.05$ for large spheres, and $2 < r < 2.05$ and $3 < r < 3.05$ for small spheres. In this way, we include the first- and second-nearet-neighbour peaks (large–large, large–small, small–large and small–small sphere pairs) as shown in figure 3. By the same reasoning for $\lambda = 4$, figure 7, we have chosen $5 < r < 5.05$ and $8 < r < 8.05$ for large spheres, and $2 < r < 2.05$ and $5 < r < 5.05$ for small spheres.

Figure 5–7 shows that the angular structures are weak. Macroscopically, this implies that there are no normal-stress differences (Brady & Bossis 1985). In figures 6 and 7, the line having the highest probability represents the higher likelihood of large spheres with other small spheres around them.

From the results shown in figures 2–7, we can conclude that for a concentrated suspension (monomodal or bimodal) under simple shearing flow, the particle doublets (large–large, large–small, or small–small spheres), triplets, etc. are formed with different configurations (linear or cyclic, depending on the concentration of the suspension) due to the lubrication forces between the 'touching' spheres.

3.2. *Average mobility at Pe* $= \infty$

The dependence of the average mobility at $Pe = \infty$, D_0^s, upon ϕ_a is reported in figure 8(*a*) for suspensions having the fraction of total solids that are small spheres, ξ, fixed at 0.27 for the size ratio of the spheres $\lambda = 1$, 2 and 4. The reported values are x- and y-averages, that is $D_0^s = \frac{1}{2}(D_{xx} + D_{yy})$, which are averaged over the last 100000 steps

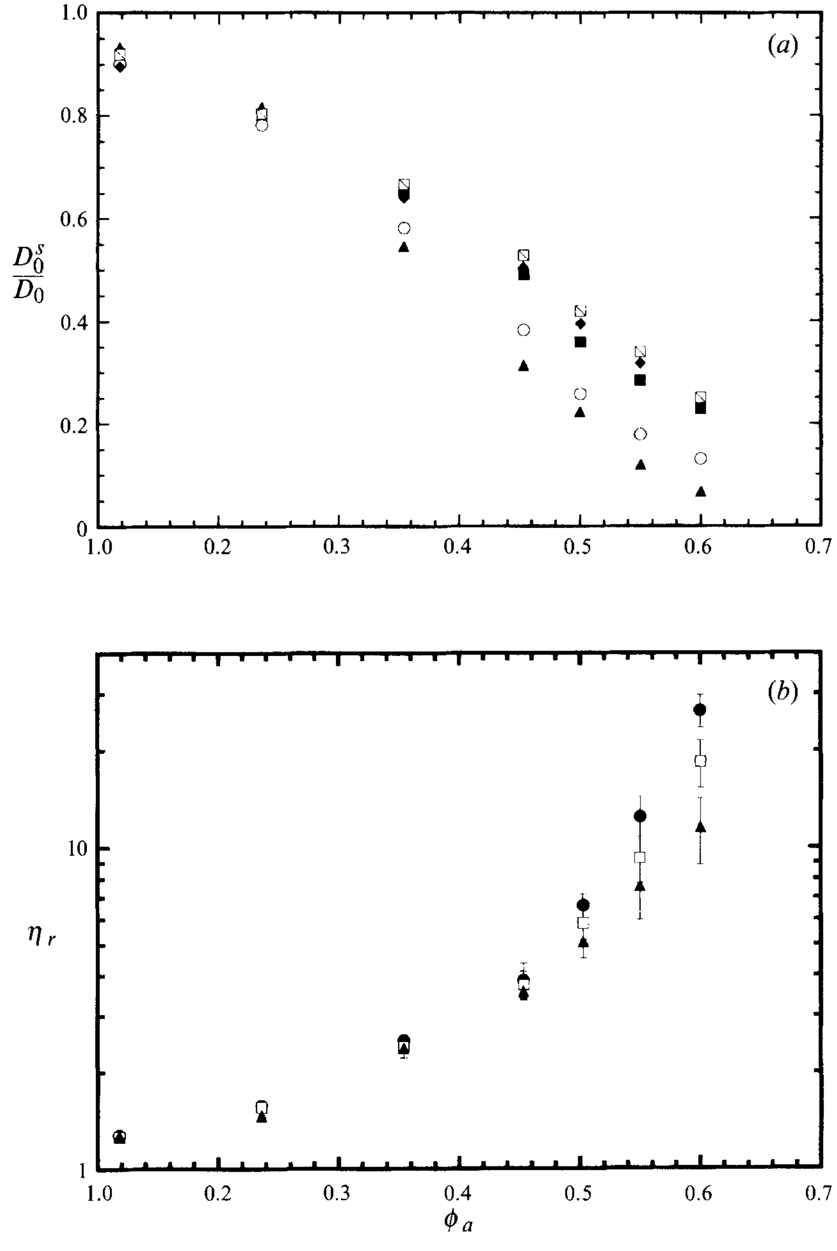

FIGURE 8. (*a*) Dependence of the average mobilities, D_0^s/D_0, on area fraction, ϕ_a, for $\lambda = 1$, 2 and 4. The fraction of small spheres is fixed at $\xi = 0.27$ for $\lambda = 2$ and 4. ■, $\lambda = 1$; ◆, large spheres, $\lambda = 2$; ○, small spheres, $\lambda = 2$; ⧅, large spheres, $\lambda = 4$; ▲, small spheres, $\lambda = 4$. (*b*) Dependence of the relative viscosities, η_r, on area fraction, ϕ_a, for $\lambda = 1$, 2 and 4. The fraction of small spheres is fixed at $\xi = 0.27$ for $\lambda = 2$ and 4. ●, $\lambda = 1$; □, $\lambda = 2$; ▲, $\lambda = 4$.

and normalized with respect to the diffusivity of a single isolated sphere. Since our bimodal suspension contain both small and large spheres, different values of D_0^s are given for each sphere size. Our result for a monodispersed suspension at $\phi_a = 0.453$ is 0.51 ± 0.02, where ± stands for the standard deviation for five different runs, which compares favourably with the value 0.57 ± 0.01 calculated by Bossin & Brady (1987). Figure 8(*a*) shows that as ϕ_a increases, D_0^s/D_0 decreases for all values of λ, where D_0

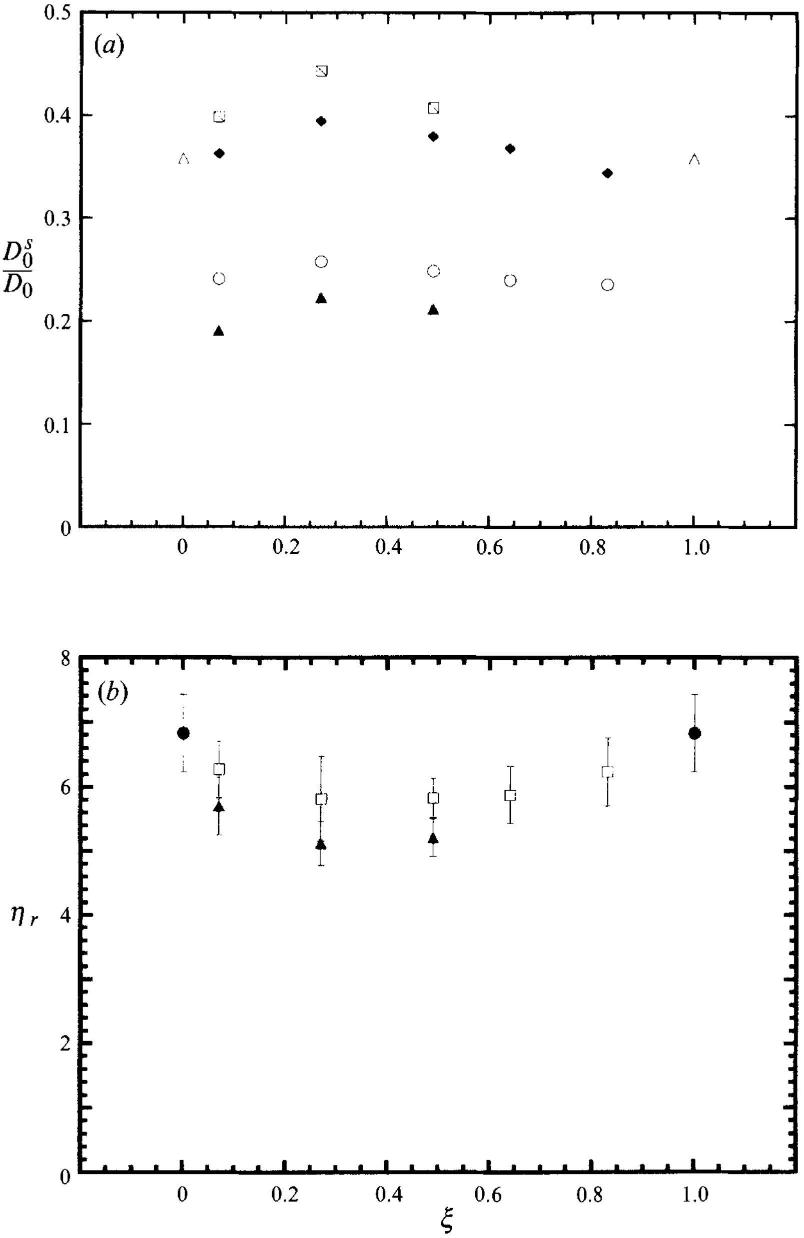

FIGURE 9. (*a*) Dependence of the average mobilities, D_0^s/D_0, on the fraction of small spheres, ξ, with area fraction, ϕ_a, fixed at 0.50. △, $\lambda = 1$; ◆, large spheres, $\lambda = 2$; ○, small spheres, $\lambda = 2$; ⧅, large spheres, $\lambda = 4$; ▲, small spheres, $\lambda = 4$. (*b*) Dependence of the relative viscosities, η_r, on the fraction of small spheres, ξ, with area fraction, ϕ_a, fixed at 0.5. ●, $\lambda = 1$; □, $\lambda = 2$; ◆, $\lambda = 4$.

is the diffusion coefficient of a single sphere at infinite dilution. That is, the particles tend to become immobilized as the concentration increases. This finding agrees with results for other transport properties. Figure 8(*b*) shows the results of Chang & Powell (1993) for the dependence of relative viscosity, η_r, on λ and ϕ_a with ξ fixed at 0.27. As ϕ_a increases, η_r increases for all values of λ owing to the distribution of cluster sizes in the suspensions. At the high concentrations the lubrication forces between particles result in the formation of large clusters concomitant with the decrease in the

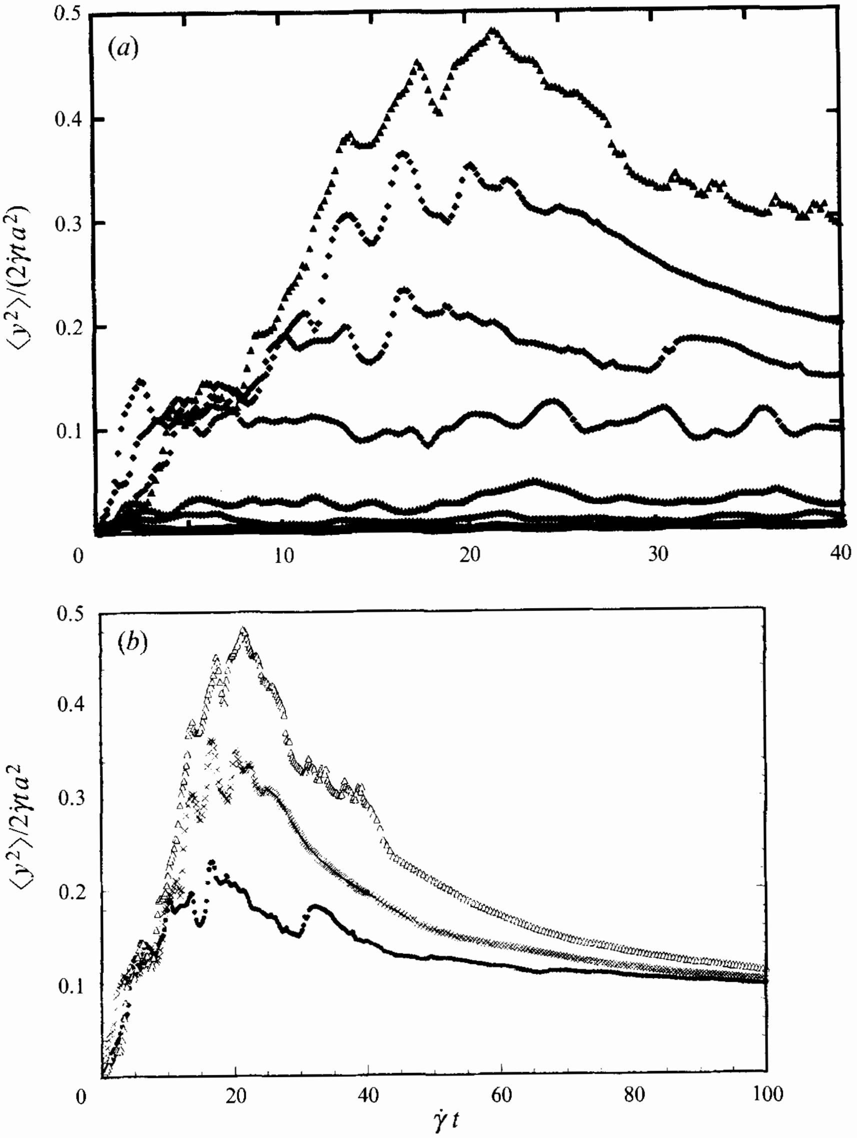

FIGURE 10. (*a*) Dependence of $\langle y^2 \rangle / 2\dot{\gamma} t a^2$ on $\dot{\gamma} t$ for monodispersed suspensions. The area fractions, ϕ_a, of the suspensions from the top curve to the bottom one are 0.60, 0.55, 0.503, 0.453, 0.354, 0.238 and 0.118, respectively. (*b*) Dependence of $\langle y^2 \rangle / 2\dot{\gamma} t a^2$ on $\dot{\gamma} t$ for $\phi_a = 0.503$ (●), 0.55 (×) and 0.60 (△) up to $\dot{\gamma} t = 100$.

instantaneous mobility of a sphere, as shown by the decrease in D_0^s. In turn, the growth in cluster size results in an increase in the viscosity of the suspension. Figure 8(*a*) also shows that for small ϕ_a (less than 0.20), D_0^s/D_0 is independent of λ and the size of the sphere. Although such suspensions are not dilute ($D_0^s/D_0 \neq 1$), this indicates that near-field particle–particle interactions are not important and hence D_0^s/D_0 should have approximately the same value for both the large and small spheres and for different values of λ. From a somewhat different viewpoint D_0^s/D_0 being the same for bimodal and monodispersed suspensions at small area fractions may result from the same scenario as that discussed in Beenakker & Mazur (1984) for Brownian particles. They used a simple model to relate the short-time diffusivity to the effective viscosity of the suspension. When the suspension is sufficiently dilute the effective viscosity is close to the Einstein viscosity, which is only a function of volume fraction and independent of size ratio. On the other hand, in concentrated suspensions, say $\phi_a > 0.55$, the particles form large clusters that contain many large and small spheres. The large cluster tends to move for a short time as if it were a single larger 'particle' and thus impart the same velocity to both the large and small spheres in the cluster. For example, at $\phi_a = 0.6$, we found that the spheres tend to form a cluster consisting of up to 80% of the spheres in the periodic cell. Both the large and small spheres in the cluster tend to move at the same velocity as the cluster. This can be shown from the data at $\phi_a = 0.6$ in figure 8(*a*), by noting that on a dimensional basis we obtain approximately the same D_0^s for both large and small spheres.

Figure 9(*a*) shows the dependence of D_0^s/D_0 on λ and ξ with ϕ_a fixed at 0.50. As ξ increases, D_0^s/D_0 increases to a maximum value and then decreases as $\xi \rightarrow 1$ for both the large and small spheres, independent of λ. The size of this effect is somewhat more pronounced for larger λ. Figure 9(*b*) shows the dependence of η_r on λ and ξ with ϕ_a fixed at 0.50 (Chang & Powell 1993). As ξ increases, η_r decreases to a minimum value and then increases as $\xi \rightarrow 1$. Figures 9(*a*) and 9(*b*) again confirm that for the same λ, the mobility of a sphere (small or large) increases as the viscosity of the suspension decreases. As described above, this can be correlated with the mean cluster size in the suspensions, or, on a macroscopic basis, we can consider that to translate a particle in a cluster one must also move the other particles in the same cluster and it is easier for a particle to move if smaller clusters are present (low concentration) rather than larger clusters (high concentration). However, our monodispersed data cannot be compared to the Monte Carlo results by Phillips *et al.* (1988) since for a Monte Carlo simulation the particles do not really follow the time evolution as in a dynamic simulation. Therefore, some essential dynamics, such as the formation of clusters as time progresses (which usually causes high viscosity), is missing when using Monte Carlo technique. This results in a lower calculated viscosity (or higher D_0^s) compared to that of a dynamic simulation (Chang & Powell 1994*a*). However, we should point out that for the short-time diffusivity at $Pe = 0$ the Monte Carlo simulation is exact (Phillips *et al.* 1988).

3.3. *Long-time self-diffusion*

The long-time self-diffusion coefficients, D_∞^s, which measure the ability of a particle to wander far from its starting point, can be determined by calculating the average particle trajectories $\langle x^2(t)\rangle$, $\langle x(t)\,y(t)\rangle$ and $\langle y^2(t)\rangle$ during a simulation. Owing to the imposed simple shearing flow, $\langle x^2\rangle$ and $\langle xy\rangle$ do not grow linearly with time, but have the following non-dimensional long-time behaviour (Bossis & Brady 1987) if the time is being measured in shear rate units $\dot{\gamma}^{-1}$ rather than in diffusion times a^2/D_0:

$$\langle x^2(t)\rangle = 2D_{xx}\,t+\tfrac{2}{3}D_\infty^s\,t^3, \qquad \langle x(t)\,y(t)\rangle = D_\infty^s\,t^2, \tag{3.2}$$

where D_{xx} is the shear-induced diffusivity in the flow direction and $D_\infty^s = D_{yy}$. The most straightforward way to determine D_∞^s is through

$$\langle y^2(t)\rangle = 2D_\infty^s\,t. \tag{3.3}$$

Equations (3.2) and (3.3) are simply the solution for the mean-square displacement of a passive diffusing scalar released at the origin in an unbounded simple shearing flow. In our simulations, these relations describe the long-time behaviour of a 'tracer' particle. The sudden jumps in position associated with the periodic boundary conditions are removed, so that the trajectories followed are those that would occur in an unbounded fluid. Bossis & Brady (1987) have shown that for a monodispersed suspension with $\phi_a = 0.453$ and $Pe \rightarrow \infty$, $\langle y^2\rangle/t$ does not reach an asymptote until the

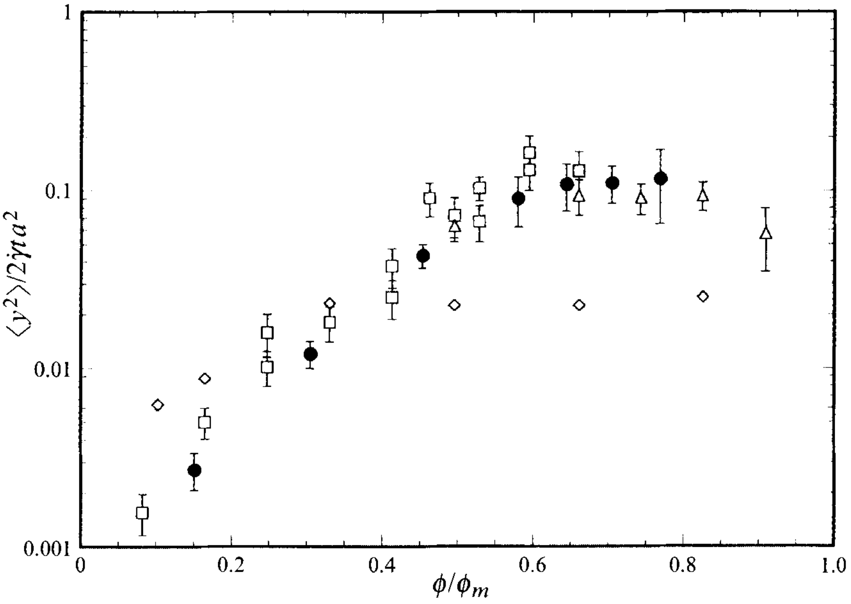

FIGURE 11. Comparison of the simulation of $\langle y^2\rangle/2\dot{\gamma}ta^2$ for monodispersed suspensions with experiment. All concentrations have been normalized by the maximum packing fraction, $\phi_m^{2d} = 0.785$ and $\phi_m^{3d} = 0.605$, to compare two- and three-dimensional results. □, Leighton & Acrivos (1987*a*); ◇, Eckstein *et al.* (1977); △, Phan & Leighton (1993); ●, present work. The error bars represent the experimental error and the statistical uncertainty in the simulations.

strain (shear rate times time) is greater than 20. This results from the formation of large clusters, encompassing most of the particles, that slowly rotate with the average angular velocity of the bulk flow and deform due to the extensional and compressional parts of the motion. As shown in figure 1(*b*), similar behaviour occurs in bimodal suspensions. The long time required to achieve steady state also indicates that the clusters display complex internal dynamics, as particles move within a cluster, but do not necessary leave it. The evolution of the clusters results in a long timescale being associated with mean particle displacements in the y-direction, especially for large ϕ_a. This is shown quantitatively in figure 10(*a*) for monodispersed suspensions, where $\langle y^2\rangle/2\dot{\gamma}ta^2$ is plotted versus $\dot{\gamma}t$, a being the particle radius, for suspensions having concentrations ranging from 0.12 to 0.60. The factor $\dot{\gamma}a^2$ is the scaling appropriate for the 'shear-induced' self-diffusion coefficient of Leighton & Acrivos (1987*a*). Our simulation results in figure 10(*a*) seem to verify the diffusive behaviour of monodispersed suspensions, although the slow evolution of cluster dynamics makes it difficult to obtain a steady state for highly concentrated suspensions, say $\phi_a \geqslant 0.5$. For example, figure 10(*b*) shows the results for $\phi_a = 0.503$, 0.55 and 0.6. The curves do not reach the asymptotic values until $\dot{\gamma}t > 50$. As ϕ_a increases from $\phi_a \rightarrow 0$, larger values of D_∞^s are expected since the tracer particle encounters more spheres which increases the mean-square displacement. But for $\phi_a \geqslant 0.5$, D_∞^s appears to approach a constant value as suggested by Phan & Leighton (1993). For $\phi_a = 0.453$, we obtain a value of $D_\infty^s/\dot{\gamma}a^2$ of 0.09. This is similar to the long-time value indicated in figure 7 of Bossis & Brady (1987). However, we do not find the peak at $\dot{\gamma}t = 4$ in their figure 7. Figure 11 compares our simulation results for $\langle y^2\rangle/2\dot{\gamma}a^2$ for monodispersed suspensions with experimental data given by Eckstein *et al.* (1977), Leighton & Acrivos (1987*a*) and Phan & Leighton (1993). In order to compare our two-dimensional simulation results with three-

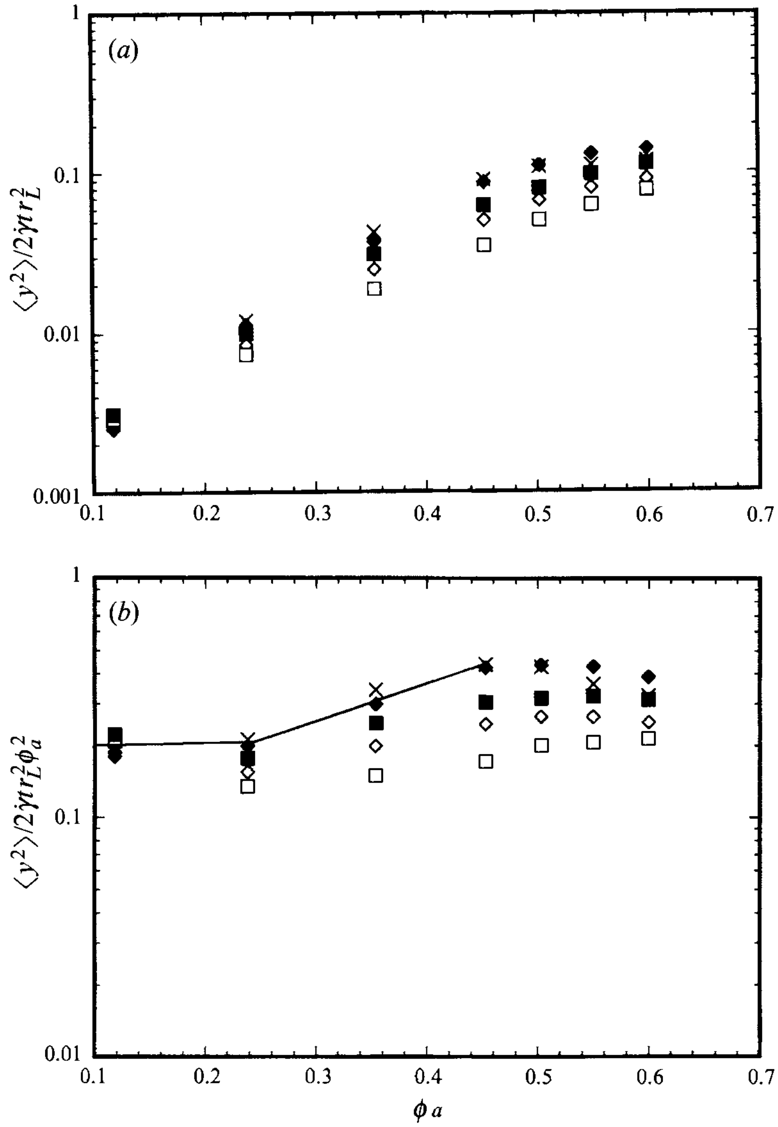

FIGURE 12. (*a*) Dependence of $\langle y^2\rangle/2\dot{\gamma}tr_L^2$ on area fraction, ϕ_a, for $\lambda = 1$, 2 and 4. The fraction of small spheres is fixed at $\xi = 0.27$ for $\lambda = 2$ and 4. ×, $\lambda = 1$; ◇, large spheres, $\lambda = 2$; ◆, small spheres, $\lambda = 2$; □, large spheres, $\lambda = 4$; ■, small spheres, $\lambda = 4$. (*b*) Dependence of $\langle y^2\rangle/2\dot{\gamma}tr_L^2\phi_a^2$ on area fraction, ϕ_a, for $\lambda = 1$, 2 and 4. Symbols in (*a*).

dimensional experimental work, all concentrations have been normalized by the two-dimensional and three-dimensional maximum packing fractions (Brady & Bossis 1985; Chang & Powell 1993), $\phi_m^{2d} = 0.785$ and $\phi_m^{3d} = 0.605$ respectively. Our results compare remarkably well with those of Leighton & Acrivos (1987*a*) and Phan & Leighton (1993). The error bars indicate experiment errors and the standard deviation derived from five different simulations with different initial conditions. We also find reasonable agreement with the results of Eckstein *et al.* (1977) at small values of ϕ_a/ϕ_m^{2d} and ϕ_v/ϕ_m^{3d}, but for large values their experiment appears to have been constrained by wall effects, leading to a reported diffusion coefficient that was much less than the correct value (Leighton & Acrivos 1987*a*).

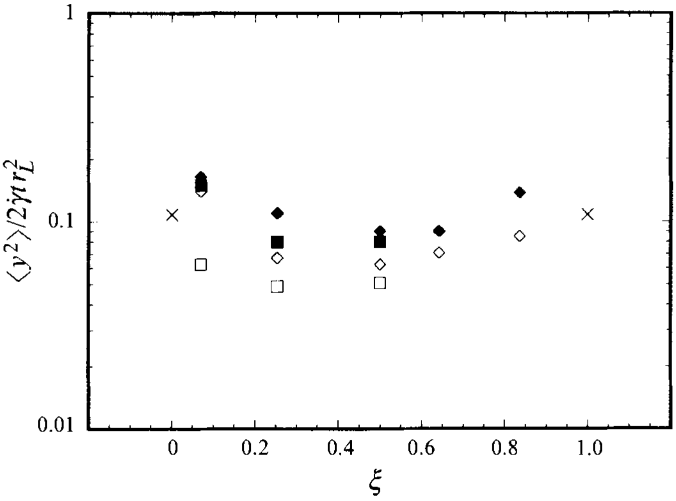

FIGURE 13. Dependence of $\langle y^2\rangle/2\dot{\gamma}tr_L^2$ on the fraction of small spheres, ξ, with area fraction, ϕ_a, fixed at 0.50. ×, $\lambda = 1$; ◇, large spheres, $\lambda = 2$; ◆, small spheres, $\lambda = 2$; □, large spheres, $\lambda = 4$; ■, small spheres, $\lambda = 4$.

	$\langle y^2\rangle/2\dot{\gamma}tr_L^2$				
ϕ_a	$\lambda = 1$	$\lambda = 2$(L)	$\lambda = 2$(S)	$\lambda = 4$(L)	$\lambda = 4$(S)
0.118	0.003	0.003	0.003	0.003	0.003
0.236	0.012	0.009	0.011	0.007	0.010
0.354	0.043	0.025	0.038	0.019	0.031
0.453	0.090	0.051	0.087	0.035	0.063
0.503	0.108	0.067	0.110	0.051	0.080
0.55	0.110	0.080	0.130	0.063	0.098
0.60	0.117	0.091	0.140	0.077	0.113

TABLE 2. The long-time diffusivities at $\xi = 0.27$ and at different fraction of total solids, ϕ_a, for $\lambda = 1$, 2 and 4 as depicted in figure 12(*a*). L denotes large spheres and S small.

Figure 12(*a*) shows the dependence of $\langle y^2\rangle/2\dot{\gamma}tr_L^2$ on the size ratio of the spheres λ and the total area fraction ϕ_a for bimodal suspensions with the fraction of total solids that are small spheres, ξ, fixed at 0.27, where r_L is the radius of the large sphere. Since for a bimodal suspension the shear-induced diffusion is caused primarily by the largest spheres in the suspension, we have non-dimensionalized the diffusivity by the radius of the large spheres. The conditions of the simulations used in this figure are the same as those in figure 8(*a*). We have tabulated in table 2 the long-time diffusivities against ϕ_a for the cases depicted in figure 12(*a*). At low concentrations, say $\phi_a < 0.2$, D_∞^s has almost the same value for both the large and small spheres, which indicates that the many-body interactions are not significant in the dilute cases. As ϕ_a increases (e.g. $\phi_a > 0.55$) the particles tend to form large clusters due to the lubrication forces and both the large and small spheres within the clusters tend to move together. Therefore, D_∞^s has similar values for the large and small spheres; however, their long-time diffusive behaviour is very different from that found at low concentrations. In order to see if our results for $\langle y^2\rangle/2\dot{\gamma}tr_L^2$ scale as ϕ_a^2, as found by Leighton & Acrivos (1987*a*), we have plotted $\langle y^2\rangle/2\dot{\gamma}tr_L^2\,\phi_a^2$ versus ϕ_a as shown in figure 12(*b*). For monodispersed suspension $\lambda = 1$, the value of $\langle y^2\rangle/2\dot{\gamma}ta^2\phi_a^2$ is about 0.2 for $\phi_a < 0.25$. In other

	$\langle y^2\rangle/2\dot{\gamma}tr_L^2$				
ξ	$\lambda = 1$	$\lambda = 2$(L)	$\lambda = 2$(S)	$\lambda = 4$(L)	$\lambda = 4$(S)
0	0.108	—	—	—	—
0.703	—	0.140	0.165	0.062	0.150
0.273	—	0.067	0.110	0.051	0.080
0.494	—	0.062	0.090	0.052	0.080
0.642	—	0.071	0.090	—	—
0.836	—	0.085	0.138	—	—
1.0	0.108	—	—	—	—

TABLE 3. The long-time diffusivities at different fraction of small spheres of solids, ξ, with $\lambda = 1$, 2 and 4 and $\phi_a = 0.503$ as depicted in figure 13

words, $\langle y^2\rangle/2\dot{\gamma}ta^2 \sim 0.2\phi_a^2$ for $\phi_a < 0.25$. If we use a simple scaling law of $\phi_a = 3/2\phi_v$ for monodispersed suspensions as suggested by Brady & Bossis (1985), then $\langle y^2\rangle/2\dot{\gamma}ta^2 \sim 0.45\phi_v^2$ for dilute suspensions. This result compares favourably with the $\langle y^2\rangle/2\dot{\gamma}ta^2 \sim 0.5\phi_v^2$ obtained by Leighton & Acrivos (1987*a*) for dilute cases.

Figure 13 shows the dependence of $\langle y^2\rangle/2\dot{\gamma}tr_L^2$ on λ and ξ with ϕ_a fixed at 0.5. The conditions of simulations were the same as those in figure 9(*a*). We have tabulated in table 3 the long-time diffusivities for the cases depicted in figure 13. As ξ increases, $\langle y^2\rangle/2\dot{\gamma}tr_L^2$ decreases to a minimum value and then increases as $\xi \rightarrow 1$ for both the large and small spheres and for different values of λ. This behaviour is similar to that found for the relative viscosity, as shown in figure 9(*b*), but opposite to that found for the average mobility, figure 9(*a*). Physically, a suspension with a lower viscosity (or higher mobility) has a smaller cluster size (Chang & Powell 1993) and therefore lower D_∞^s. As discussed above, for monodispersed suspensions D_∞^s increases as ϕ_a increases from low concentration (small cluster size) to high concentration (large cluster size). By the same token, in bimodal suspensions a tracer particle encounters many more spheres in a system with large clusters, and thus has a higher mean-square displacement, $\langle y^2\rangle$, than in a system with small clusters.

Figure 14 shows that $\langle xy\rangle/t^2$ and $\langle x^2\rangle/t^3$ gave statistically the same diffusivities as $\langle y^2\rangle/t$ for both $\lambda = 1$ and 2, indicating the correctness of (3.2) and (3.3) (Bossis & Brady 1987). Figure 14(*a*) shows D_∞^s versus $\dot{\gamma}t$ for $\lambda = 1$ with $\phi_a = 0.50$, where $\langle x^2\rangle$, $\langle xy\rangle$ and $\langle y^2\rangle$ have reached the same value when the strain is greater than 20. Figures 14(*b*) and 14(*c*) show D_∞^s versus $\dot{\gamma}t$ for $\lambda = 2$, $\xi = 0.27$ and $\phi_a = 0.50$, for both the large and small spheres respectively. Similar to the monodispersed case, D_∞^s attains the same value for all $\langle x^2\rangle$, $\langle xy\rangle$ and $\langle y^2\rangle$ when $\dot{\gamma}t > 20$. In obtaining figures 14(*a*)–14(*d*), we performed five simulations using different initially homogeneous random configurations and averaged them for each case of $\lambda = 1$ and $\lambda = 2$. We found that D_∞^s was reproducible from run to run and determined the same values for $\langle x^2\rangle$, $\langle xy\rangle$ and $\langle y^2\rangle$.

3.4. *Diffusion in bimodal suspensions with an initially organized configuration*

For all of the results reported above, the simulations were begun by randomly distributing the spheres in a unit cell, figure 1(*a*). Since the long-time results should be independent of the initial configuration, we undertook some calculations to test this. Figure 15(*a*) shows a highly organized initial configuration. The large spheres rest mainly in the upper half of the unit cell while the small spheres are in the lower half. One row of spheres contains both large and small spheres. The columns are arranged so that the particle centres are aligned except for one 'defect' involving a small sphere

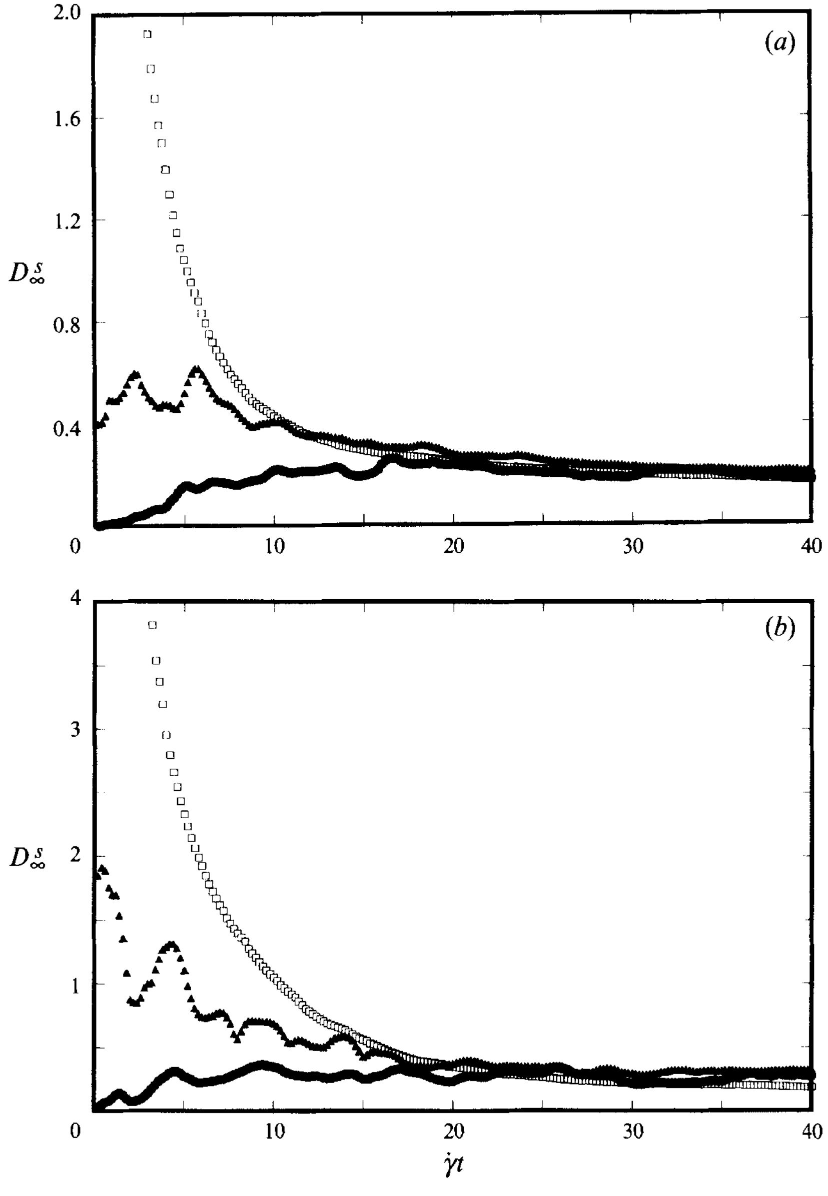

FIGURE 14(*a*, *b*). For caption see facing page.

near the centre of the unit cell. For this simulation, $N_l = 20$, $N_s = 29$, $\lambda = 2$, $\phi_a = 0.5$ and $\xi = 0.27$. Simple shearing occurs for $\dot{\gamma}t > 0$. As with the other simulations, particles tended to form clusters, due to the lubrication forces. At $\dot{\gamma}t = 10$, or after 5×10^4 time steps, the separation between the large and small spheres remains, although some large spheres have been dispersed into the bottom region and some small spheres have moved to the top region of the periodic cell. One should note here, however, that owing to the use of periodic boundary conditions, the three small spheres on the top can have migrated either from the bottom half of the cell shown or from the adjacent cell above. Likewise, the two large spheres at the bottom might have moved into the periodic cell from the cell immediately below. As time progresses further homogenization occurs, involving both large and small spheres. By $\dot{\gamma}t = 20$, some

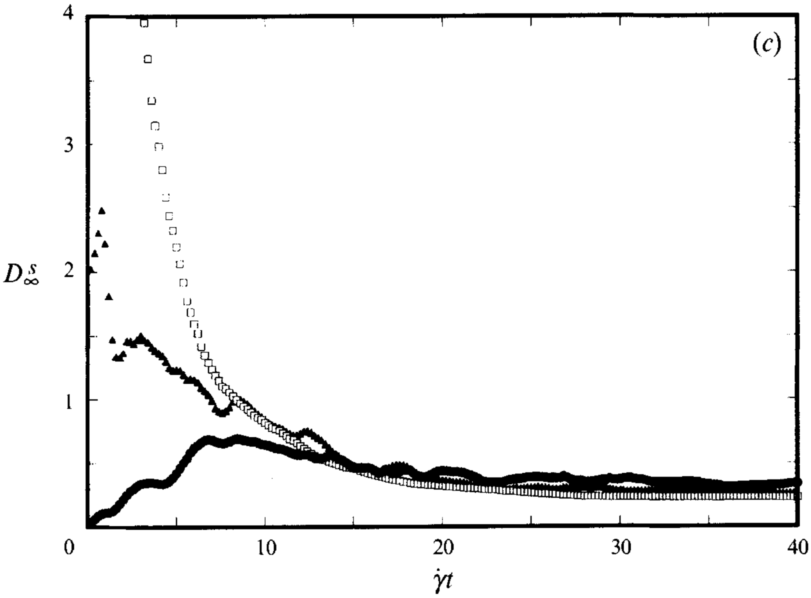

FIGURE 14. Dependence of the long-time self-diffusion coefficients, D^s_∞, on shear strain, $\dot{\gamma}t$, for $\langle xx \rangle$, $\langle xy \rangle$ and $\langle yy \rangle$ as defined in (3.4) and (3.5). (*a*) $\lambda = 1$ with $\phi_a = 0.50$; (*b*) large spheres, $\lambda = 2$ with $\phi_a = 0.50$ and $\xi = 0.27$; (*c*) small spheres, $\lambda = 2$ with $\phi_a = 0.50$ and $\xi = 0.27$. □, $\langle xx \rangle$; ▲, $\langle xy \rangle$; ●, $\langle yy \rangle$.

small spheres fill the gaps between large spheres and the particles have formed large clusters that are more compact than at $\dot{\gamma}t = 10$. After $\dot{\gamma}t > 30$ (say $\dot{\gamma}t \approx 40$), owing to the continuous formation and breakup of large clusters in shearing flow field, there seems to be more small spheres in the upper region of the periodic cell than at the lower portion. The reason for that might be the rotation of the large clusters, which 'ejects' small spheres belonging to it in the bottom region into the neighbouring cell. The images of these 'missing' spheres would enter the central periodic cell from the upper cell, and hence increase the concentration of small spheres in the upper region. Figures 15(*b*) and 15(*c*) show $\langle p(r) \rangle_\theta$ for a reference large and small sphere, respectively. The data, which were calculated using $\dot{\gamma}t = 20$ to $\dot{\gamma}t = 30$, show that a large sphere has a higher chance of finding another large sphere next to it, and a small sphere has a higher probability of finding small spheres surrounding it. Compared to figures 3(*a*) and 3(*b*), this indicates that the steady state has not yet been reached at $\dot{\gamma}t = 30$. Yet, the calculation of $\langle p(r) \rangle_\theta$ from $\dot{\gamma}t = 30$ to $\dot{\gamma}t = 40$ shows similar results to figures 3(*a*) and 3(*b*), which indicates that the steady state can be reached after $\dot{\gamma}t > 30$.

Figure 16 compares the time evolution of $\langle y^2 \rangle / 2\dot{\gamma}tr_L^2$ for initially homogeneous and random, and initially organized suspensions, for $\lambda = 2$, $\phi_a = 0.5$ and $\xi = 0.27$. For both initial conditions, both the large (figure 16*a*) and small (figure 16*b*) spheres achieve diffusive behaviour at long times. There is a slight tendency for the initially organized configuration to require a longer time ($\dot{\gamma}t > 30$) than needed by the initially randomly dispersed suspension ($\dot{\gamma}t > 20$). Further, the initially organized suspension approaches asymptotic behaviour more or less monotonically. A similar result was found for a suspension with $\lambda = 4$, $\phi_a = 0.5$ and $\xi = 0.27$, only in this case both the large and small spheres need an even longer time to attain the asymptotic diffusive behaviour ($\dot{\gamma}t > 40$) for the initially organized suspension as compared with the time required by the initially homogeneous random configuration ($\dot{\gamma}t > 20$).

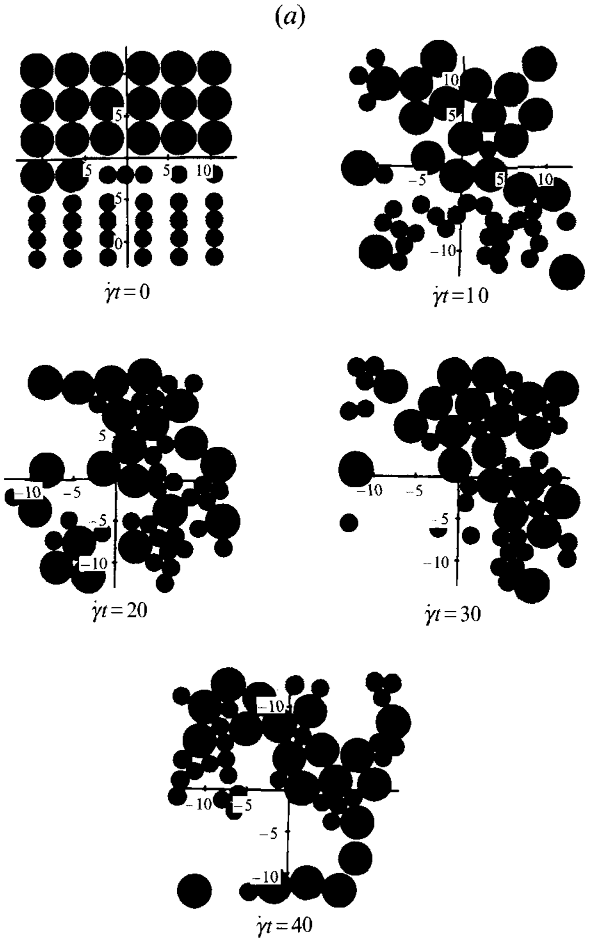

$\dot{\gamma}t=0$ $\dot{\gamma}t=10$ $\dot{\gamma}t=20$ $\dot{\gamma}t=30$ $\dot{\gamma}t=40$

FIGURE 15(*a*). For caption see facing page.

4. Conclusions

We have extended the general method of Stokesian dynamics to compute both the microstructure (pair-connectedness functions) and the macroscopic transport properties (average mobilities and long-time self-diffusion coefficients) of bimodal suspensions of hydrodynamically interacting spherical particles. To minimize computation costs while maintaining the pertinent hydrodynamics in the plane of shear, we simulated the flow of a monolayer of spheres with their centres coplanar. We replicated a unit cell containing N particles using periodic boundary conditions and so represented an infinite suspension.

Cluster formation, a direct result of the hydrodynamic lubrication forces that keep particle surfaces from touching, provided a mechanism for the calculated reduction of D_0^s, the measure of the average mobility of a particle in a local structure, as ϕ_a increases. Based upon our earlier results (Chang & Powell 1993), we can link this reduction of D_0^s to an increase in the relative viscosity caused by the formation of large clusters in the suspension. This analogy carries over to the bimodal case where there is a direct correlation among high D_0^s, low η_r and small average clusters. For long-time self-diffusivity, D_∞^s, our simulations agree remarkably well with the experiments of Leighton & Acrivos (1987*a*) and Phan & Leighton (1993) for monodispersed

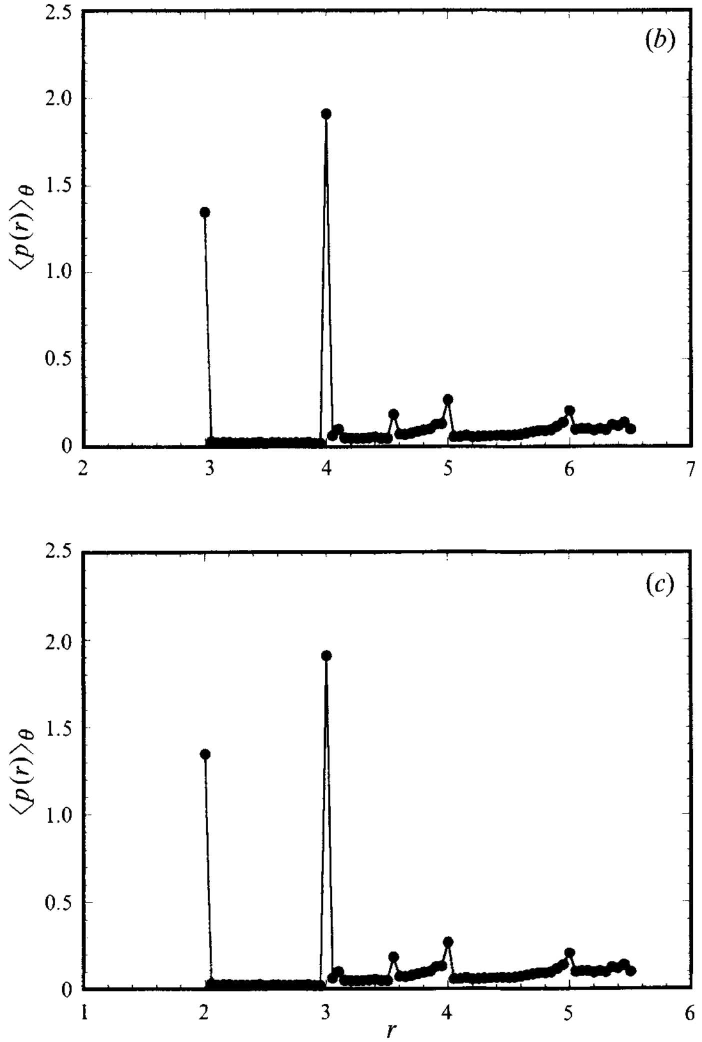

FIGURE 15. (*a*) The time evolution of the microstructure of an initially organized bimodal suspension at $\dot{\gamma}t = 0$ (initial condition), 10, 20, 30 and 40. The total area fraction is 0.50 with $\xi = 0.27$ and $\lambda = 2$. There are 20 large spheres and 29 small spheres in the periodic cell. The central periodic cell (refer to figure 1) is shown. (*b*) $\langle p(r)\rangle_\theta$ relative to a large sphere. (*c*) $\langle p(r)\rangle_\theta$ relative to a small sphere.

suspensions. For bimodal suspensions, the magnitude of D^s_∞ and the time to reach the asymptotic diffusive behaviour depend on the cluster sizes formed in the system (or the viscosity of a suspension). As ϕ_a increases, longer times are needed for both the large and small spheres to behave diffusively, a phenomenon similar to the monodispersed case.

A comparison of D^s_∞ was made for suspensions which are physically similar (same λ, ϕ_a and ξ), but with initially different microstructures. A suspension with an initially organized configuration requires a longer time for a sphere to attain diffusive behaviour than an initially homogeneous and random suspension. This probably arises from the very high local concentration in the region with large spheres introduced in the initial condition (see figure 15), which inhibits the ability of the particles to diffuse. Although experimental data are needed to verify our results, the present work shows

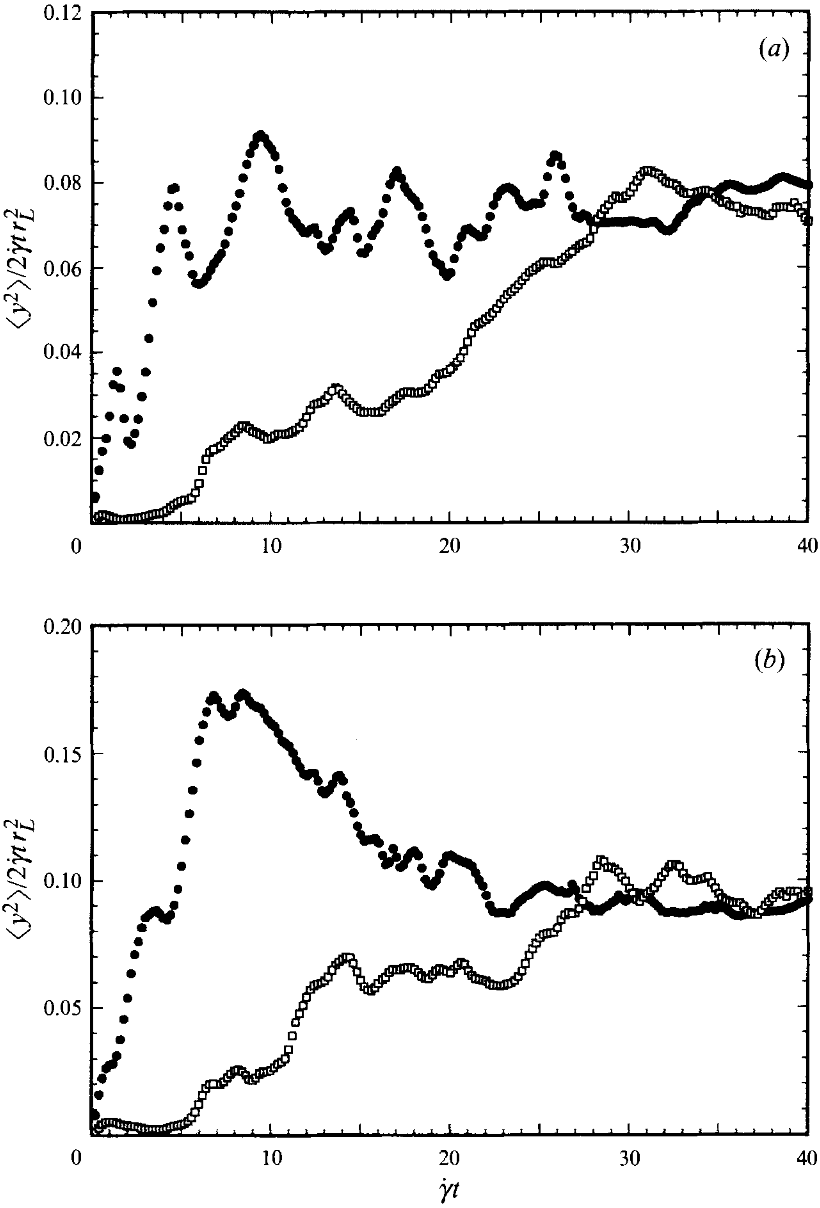

FIGURE 16. Dependence of $\langle y^2\rangle/2\dot{\gamma}tr_L^2$ on $\dot{\gamma}t$ for bimodal suspensions ($\lambda = 2$) with initially random and initially organized configurations. The total area fraction is 0.50 with $\xi = 0.27$. For both cases, there are 20 large spheres and 29 small spheres in the periodic cell. (*a*) Large spheres in initially random configuration (●), and initially organized configuration (□); (*b*) small spheres in initially random configuration (●) and initially organized configuration (□).

the ability of the Stokesian dynamics to handle diffusive effects in suspensions of unequal-sized spheres, as well as providing a thorough understanding of how the fundamental mechanisms operating on the microscale affect this behaviour.

This work was supported by the Chemical Systems Division (CSD) of United Technologies. We thank Dr R. R. Miller of CSD for his encouragement, support and thoughtful comments. The authors wish to thank Professor John Brady for his help in initiating this study. Professors David Jeffrey and Sangtae Kim graciously allowed us to see early versions of manuscripts that also became central to our research. We would also like to thank Dr R. J. Phillips for helpful discussions.

REFERENCES

ABBOTT, J. R., TETLOW, N., GRAHAM, A. L., ALTOBELLI, S. A., FUKUSHIMA, E., MONDY, L. A. & STEPHENS, T. S. 1991 Experimental observations of particle migration in concentrated suspensions: Couette flow. *J. Rheol.* **35**, 773–795.

BATCHELOR, G. K. 1976 Brownian diffusion of particles with hydrodynamic interaction. *J. Fluid Mech.* **75**, 1–29.

BATCHELOR, G. K. & GREEN, J. T. 1972 The hydrodynamic interaction of two small freely-moving spheres in a linear flow field. *J. Fluid Mech.* **56**, 375–400.

BEENAKKER, C. W. J. & MAZUR, P. 1984 Diffusion of spheres in a concentrated suspension II. *Physica* A **126**, 349–370.

BOSSIS, G. & BRADY, J. F. 1984 Dynamic simulation of sheared suspensions. I. General Method. *J. Chem. Phys.* **80**, 5141–5154.

BOSSIS, G. & BRADY, J. F. 1987 Self-diffusion of Brownian particles in concentrated suspensions under shear. *J. Chem. Phys.* **87**, 5437–5448.

BOSSIS, G. & BRADY, J. F. 1989 The rheology of Brownian suspensions. *Chem. Phys.* **91**, 1866–1874.

BOSSIS, G. & BRADY, J. F. 1990 Diffusion and rheology in concentrated suspensions by Stokesian dynamics. In *Hydrodynamics of Dispersed Media* (ed. J.-P. Hulin, A. M. Cazabat, E. Guyon & F. Carmona). Elsevier.

BRADY, J. F. & BOSSIS, G. 1985 The rheology of concentrated suspensions of spheres in simple shear flow by numerical simulation. *J. Fluid Mech.* **155**, 105–129.

BRADY, J. F. & BOSSIS, G. 1988 Stokesian dynamics. *Ann. Rev. Fluid Mech.* **20**, 111–157.

BRADY, J. F., PHILLIPS, R. J., LESTER, J. C. & BOSSIS, G. 1988 Dynamic simulation of hydrodynamically interacting suspensions. *J. Fluid Mech.* **195**, 257–280.

CARNAHAN, B., LUTHER, H. A. & WILKES, J. O. 1969 *Applied Numerical Methods*. John Wiley & Sons.

CHANG, C. 1993 The rheology of bimodal suspensions of hydrodynamically interacting spherical particles. PhD thesis, University of California at Davis.

CHANG, C. & POWELL, R. L. 1993 Dynamic simulation of bimodal suspensions of hydrodynamically interacting spherical particles. *J. Fluid Mech.* **253**, 1–25.

CHANG, C. & POWELL, R. L. 1994*a* The rheology of bimodal hard-sphere dispersions. *Phys. Fluids*, **6**, 1628–1636.

CHANG, C. & POWELL, R. L. 1994*b* Calculation of the grand mobility functions for two unequal rigid spheres in low-Reynolds-number flow by the multipole-moment method. *Particulate Sci. Technol.* (to appear).

CHONG, J. S., CHRISTIANSEN, E. B. & BAER, A. D. 1971 Rheology of concentrated suspensions. *J. Appl. Polymer Sci.* **15**, 2007–2021.

DURLOFSKY, L. & BRADY, J. F. 1989 Dynamic simulation of bounded suspensions of hydrodynamically interacting particles. *J. Fluid Mech.* **200**, 39–67.

DURLOFSKY, L., BRADY, J. F. & BOSSIS, G. 1987 Dynamic simulation of hydrodynamically interacting particles. *J. Fluid Mech.* **180**, 21–49.

ECKSTEIN, E. C., BAILEY, D. G. & SHAPIRO, A. H. 1977 Self-diffusion of particles in shear flow of a suspension. *J. Fluid Mech.* **79**, 191–208.

EVANS, D. J. 1979 The frequency dependent shear viscosity of methane. *Molec. Phys.* **37**, 1745–1754.

FIJNAUT, H. M. 1981 Wave vector dependence on the effective diffusion coefficient of Brownian particles. *J. Chem. Phys.* **74**, 6857–6863.

GADALA-MARIA, F. & ACRIVOS, A. 1980 Shear-induced structure in a concentrated suspension of solid spheres. *J. Rheol.* **24**, 799–814.

GAWLINSKI, E. T. & STANLEY, H. E. 1981 Continuum percolation in two dimensions: Monte Carlo tests of scaling and universality for non-interacting discs. *J. Phys.* A: *Math. Gen.* **14**, L291–L299.

GLENDINNING, A. B. & RUSSEL, W. B. 1982 A pairwise additive description of sedimentation and diffusion in concentrated suspensions of hard spheres. *J. Colloid Interface Sci.* **89**, 124–143.

GRAHAM, A. L., ALTOBELLI, S. A., FUKUSHIMA, E., MONDY, L. A. & STEPHENS, T. S. 1991 Note: NMR imaging of shear-induced diffusion and structure in concentrated suspensions undergoing Couette flow. *J. Rheol.* **35**, 191–201.

HOSHEN, J. & KOPELMAN, R. 1976 Percolation and cluster distribution. I. Cluster multiple labeling technique and critical concentration algorithm. *Phys. Rev.* B **14**, 3438–3445.

JEFFREY, D. J. 1992 The extended resistance functions for two unequal rigid spheres in low-Reynolds-number flow. *Phys. Fluids* A **4**, 16–29.

JEFFREY, D. J. & ONISHI, Y. 1984 Calculation of the resistance and mobility functions for two unequal rigid spheres in low-Reynolds-number flow. *J. Fluid Mech.* **139**, 261–290.

KIM, I. C. & TORQUATO, S. 1990 Monte Carlo calculations of connectedness and mean cluster size for bidispersions of overlapping spheres. *J. Chem. Phys.* **93**, 5998–6002.

KIM, S. & KARRILA, S. J. 1991 *Microhydrodynamics: Principles and Selected Applications.* Butterworth-Heinemann.

KOCH, D. L. 1989 On hydrodynamic diffusion and drift in sheared suspensions. *Phys. Fluids* A **1**, 1742–1745.

LEE, S. B. & TORQUATO, S. 1988 Pair connectedness and mean cluster size for continuum-percolation models: Computer-simulation results. *J. Chem. Phys.* **89**, 6427–6433.

LEIGHTON, D. & ACRIVOS, A. 1987*a* Measurement of self-diffusion in concentrated suspensions of spheres. *J. Fluid Mech.* **177**, 109–131.

LEIGHTON, D. & ACRIVOS, A. 1987*b* The shear-induced migration of particles in concentrated suspensions. *J. Fluid Mech.* **181**, 415–439.

MILLER, R. R., LEE, E. & POWELL, R. L. 1991 Rheology of solid propellant dispersions. *J. Rheol.* **35**, 901–920.

NADIM, A. 1988 The measurement of shear-induced diffusion in concentrated suspensions with Couette device. *Phys. Fluids* **31**, 2781–2785.

O'BRIEN, R. W. 1979 A method for the calculation of the effective transport properties of suspensions of interacting particles. *J. Fluid Mech.* **19**, 17–39.

OTTEWILL, R. H. & WILLIAMS, N. ST. J. 1987 Study of particle motion in concentrated dispersions by tracer diffusion. *Nature* **325**, 232–234.

PHAN, S. E. & LEIGHTON, D. 1993 Measurement of the shear-induced tracer diffusivity in concentrated suspensions. *J. Fluid Mech.* (submitted).

PHILLIPS, R. J., ARMSTRONG, R. C., BROWN, R. A., GRAHAM, A. L. & ABBOTT, J. R. 1992 A constitutive equation for concentrated suspensions that accounts for shear-induced particle migration. *Phys. Fluids* A **4**, 30–40.

PHILLIPS, R. J., BRADY, J. F. & BOSSIS, G. 1988 Hydrodynamic transport properties of hard-sphere dispersions. I. Suspensions of freely mobile particles. *Phys. Fluids* **31**, 3462–3472.

PUSEY, P. N. & VAN MEGEN, W. J. 1983 Measurement of the short-time self-mobility of particles in concentrated suspension. Evidence of many-particle hydrodynamic interactions. *J. Phys. Paris* **44**, 285–291.

RALLISON, J. M. & HINCH, E. J. 1986 The effect of particle interactions on dynamic light scattering from a dilute suspension. *J. Fluid Mech.* **167**, 131–168.

SEATON, N. A. & GLANDT, E. E. 1987 Aggregation and percolation in a system of adhesive spheres. *J. Chem. Phys.* **86**, 4668–4677.

SEVICK, E. M., MONSON, P. A. & OTTINO, J. M. 1988 Monte Carlo calculations of cluster statistics in continuum models of composite morphology. *J. Chem. Phys.* **88**, 1198–1206.

VAN MEGEN, W., UNDERWOOD, S. M. & SNOOK, I. 1986 Tracer diffusion in concentrated colloidal dispersions. *J. Chem. Phys.* **85**, 4065–1072.

WEINBAUM, S., GANATOS, P. & YAN, Z. Y. 1990 Numerical multipole and boundary integral equation techniques in Stokes flow. *Ann. Rev. Fluid Mech.* **22**, 275–316.